Time Averaged Potentials in Ioffe-Quadrupole traps and Zeeman Sideband Spectroscopy

Tobias Gerard Tiecke
July 2002

Thesis for graduation in experimental physics
at the University of Amsterdam
Supervisor:
Wolf von Klitzing

Working group of: Prof. Dr. J.T.M. Walraven
FOM Institute for Atomic and Molecular Physics, Amolf
Amsterdam

Abstract

This thesis describes the project done for the graduation in experimental physics at the University of Amsterdam. The report is twofold. We present the development of a new type of spectroscopy. This *Zeeman sideband spectroscopy* is based on modulating the magnetic field in a gaseous sample. The laser has been found to be stable, less sensitive to external drifts as compared to previously known types of spectroscopy, narrow bandwidth and cost effective. Based on this type of spectroscopy we present a frequency stabilized laser source to be used in BEC experiments. In the second part we present a model describing the magnetic trapping potential. The algebraic model based on numerical calculations, is found to be extremely useful for the experiments done. We present a new type of TOP trap realized in a Ioffe-Quadrupole trap. As an application we present the first realization of two BEC's in a purely magnetic Ioffe-Quadrupole trap. As a demonstration of the possibilities we briefly show the collisional process of two BEC's.

Contents

General Introduction

Chapter 1

Bose Einstein Condensation

1.1   Historical

Bose Einstein Condensation (BEC) has been predicted by Einstein in the early 20's [2] on the basis of the work of Bose [1]. The phenomenon is based on the wave nature and bosonic properties of atoms. If an gas is cooled this implies that its thermal velocity becomes lower. The Heisenberg relation states that the uncertainty in the place and velocity are coupled. Therefore a lower, thus better determined, thermal velocity implies a higher uncertainty in the position. The uncertainty in the position is characterized by the thermal de Broglie wavelength given by:

$$\Lambda_T = \sqrt{\frac{2\pi\hbar^2}{mk_BT}}.$$
(1.1)

Einstein stated that a phase transition occurs when this uncertainty becomes of the interatomic spacing. The critical temperature at which the condensation occurs follows from the criterium:

$$n(0)\Lambda_T^3 = \zeta(3/2) = 2.612...,$$
(1.2)

where $n(0)$ is the density and $\zeta(3/2)$ the Riemann Zeta function. For atomic gasses the critical temperature is at extremely low values. For example for ^{87}Rbthe critical temperature is $1\,\mu$K at a density of $10^{14}\,$cm^{-3}. In the past decades technical developments, most notably laser cooling of alkali atoms, have made it possible to realize these densities and temperatures. This led to the first BEC realized at JILA by Cornell and Wiemann [3].
This enabeled a new elan of experiments exploring the properties of macroscopic quantum object.

1.2 Apparatus needed to achieve BEC

To achieve the high densities and low temperatures stated above a number of different types of apparatus have to be used. Bose Einstein Condensates are generally realized by means of optical cooling Magneto Optical Traps (MOT)[1], magnetic traps and evaporative cooling. A Magneto Optical Trap is a combination of a magnetic and optical potential confining the atoms. This combination has proven to provide the desired cooling and confinement.

The condensation scheme as used at the Amolf institute consists of the following steps: $4 \cdot 10^9$ atoms are loaded into the magneto optical trap and subsequently transferred to the magnetic trap. By increasing the confinement by the magnetic trapping potential the cloud is compressed to higher densities ($\sim 7 \cdot 10^{11}\,\mathrm{cm}^{-3}$). The last step in the process to obtain a BEC is evaporative cooling. This consists of selectively removing the highest energy atoms from the trap. In this process the density of the cloud is further increased and the temperature is lowered. After this stage a BEC is obtained in the trap.
A measurement of a BEC is generally done by switching the trapping potential off and taking an absorption image of the cloud in free flight. Such a measurement consists of flashing a laser beam with a frequency (slightly off) resonant to a transition in the atom. A picture of the shadow of the condensate is then taken with a CCD camera. This light destroys the condensate but the information about the atom distribution is obtained[2].

1.3 This project

This thesis describes the graduation project done at the Amolf institute. The work consists of two parts: one describing a newly built laser system and one of the modelling of the magnetic trapping potential.

Laser system As explained above lasers are used for trapping and cooling atoms to obtain a BEC. The requirements for this type of lasers are very high. At the Amolf institute the Bose Einstein Condensates consist of rubidium-87 atoms. The natural linewidth of the transitions in rubidium is about $6\,\mathrm{MHz}$. To be able to perform accurate measurements a laser with the stability of the order of $1\,\mathrm{MHz}$ is favorable. A frequency stability of that order enables the possibility to tune the laser on or off a resonant transition. This property is mandatory for efficient trapping and detection of atoms.
The stabilization of the frequency is performed by external locking to an absolute frequency measure. Atomic transitions in rubidium are used as an absolute

---

[1]The realization of a purely optical BEC has been reported by Barrett, et. al. [4]

[2]Another method used is *phase contrast imaging*. This provides the possibility to observe the condensate in situ without destroying the condensate.

frequency measure.

In this report we will describe the development of a new frequency stabilized laser source. This is based on a newly developed type of spectrometer which will be presented.

Magnetic trap　The quantum nature of Bose Einstein Condensates gives rise to various interesting phenomena. Due to the macroscopic nature these quantum mechanical effects become observable.

By modulating the magnetic trapping potential one can manipulate a trapped BEC. In this manner a BEC can be excited in various states. The research into manipulating BEC's, for example vortex formation and oscillation modes, is currently a very active field. A part of the research program at the Amolf institute consists of examining condensate shape oscillations. For this purpose a model of the trapping potential has been developed. This model is an algebraic model with numerically derived coefficients. The model has gained new insight in the possibilities of manipulating condensates in Ioffe-Quadrupole type of traps. The first realization of two purely magnetic trapped condensates in a Ioffe-Quadrupole trap will be presented.

Part I

Spectroscopy

Chapter 2

Diode Lasers

2.1 Introduction

The development of the laser started in 1917 when Einstein proposed stimulated emission. Based upon the techniques realized in masers in the 50's (for which Townes, Basov and Prokhorov received the Nobel Prize in 1964) it took until 1958 when Townes and Schawlow proposed a technique for a monochromatic coherent light source [5]. Two years later Maiman realized the first optical maser (laser) in ruby. Maiman's paper submitted to Physical Review Letters was rejected and the first publication was a small article in Nature in August 1960 [6]. After this first realization lasers rapidly became a widely used tool in research labs. In 1970 with the realization of the first continuous diode laser lasers became a more reliable, cheap and easy to operate tool for fundamental research. This ease of use made lasers also more applicable for commercial purposes (eg. CD-players).

Tunable lasers enabled more possibilities in a wide range of experiments. In atom-physics narrow linewidths are mandatory. Gas lasers width a linewidth as low as $0.01Hz$ have been reported in literature[7]. However, they lack in tunability and ease of use. Diode lasers provide the flexibility but the linewidth is larger ($\Delta f \sim 50\text{MHz}$). Temperature changes or current-density changes influence the internal cavity of the diode largely. Consequently the resonant frequency can be shifted over a large frequency range. A more detailed description on diode lasers can be found in [8].

A common method to narrow the linewidth of a diode laser will be explained in the following paragraph.

2.2 Grating stabilized lasers

As pointed out above for diode lasers to be applicable to atom-physics one needs to narrow the linewidth. A common method is to place a grating in front of the diode. The grating is placed under an angle as can be seen in figure 2.1. The angle is such that the strongest order reflection of the desired frequency is reflected back into the diode. This setup is known as the Littrow setup.
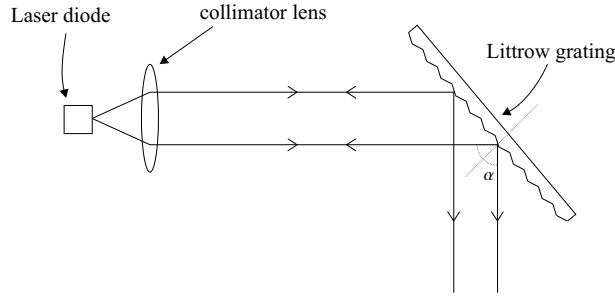
Figure 2.1: *A schematic representation of the Littrow setup. The Littrow grating is a grating blazed at the desired angle. In our case α is about 45°. The grating is aligned such that the strongest order is reflected back into the laser diode. This creates a extended cavity. The second strongest order reflection is sent to the rest of the setup.*

The grating selectively reflects the desired frequency from the broad spectral range emitted by the diode. The reflected frequency is determined by: $\sin \alpha = k\lambda/2d$, where α is the angle at which the grating is placed, k is the diffraction order (generally the first order), λ the wavelength of the selected frequency and d the grating constant. The wavelength selected by the angle of the grating is fed back into the diode. If the gain is then above unity the diode will lase at this frequency as well as its bandwidth.

Four factors determine the frequency at which the grating stabilized laser lases, first there is the gain profile. This is typically of the order of 5000 GHz for the diodes used in our experiments. It can be shifted by changing the current density or the temperature. Second there is the reflectivity of the grating back to the diode. This is referred to as the grating profile. Its width can be calculated from the formula: $\Delta\nu_g \simeq c/(\lambda n L_g)$ where λ is the wavelength of the first order reflection, L_g the illuminated grating length, n the order of the reflection and c the speed of light. This results for our setup in $\Delta\nu_g \simeq 50$ GHz. Finally there are the two cavities. First the internal cavity created by the two facets of the diode. The free spectral range (spacing of the modes) is in our case measured to be ~ 64 GHz. Second there is the cavity spanned between the diode and the grating. According to: $FSR_{ext} = c/(2L_{ext})$ this is calculated to be 9.4 GHz with L_{ext} the external cavity length ($\simeq 16$ mm). The relative width of the four bandwidth factors is illustrated in figure 2.2. The resulting bandwidth is

typically of the order of a few 100 kHz's.
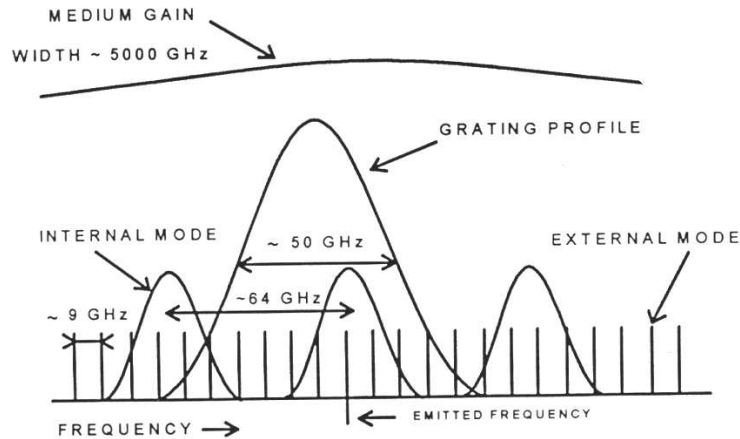
Figure 2.2: *The final bandwidth of a grating stabilized laser is determined by four aspects. The gain profile (denoted as the* medium gain*), the grating profile and the free spectral ranges of the diode and the extended cavity (denoted as* internal mode *and* external mode*). From these factors the emitted frequency can be determined.*

The second strongest reflection of the grating is used as a source (see figure 2.1). In this manner a narrow linewidth laser source is obtained.

The frequency of the grating stabilized laser can be adjusted by changing the angle of the grating. In combination with changing the temperature and the current of the diode one can obtain a frequency tunability over more than the whole gain profile of the diode (typically of the order of $5000\,\mathrm{GHz}$). Due to the sensitivity with respect to the temperature and the current of the diode one needs to stabilize the temperature and the current the diode is being operated at. An absolute measure of the frequency is also needed for long term stabilization. This will be explained in the next chapter.

2.2.1 Injection locking of lasers

A narrow linewidth and adjustable frequency source can be achieved as seen above. By using a grating to select a frequency much power is lost. To obtain the desired amount of power an optical amplifier is needed. This can be achieved by injection locking a second laser diode. The light from the grating stabilized laser (the master laser) is fed into the second laser diode (the slave laser). The preferred mode in the slave laser will be the one injected by the master laser. The full power of the slave laser can thus be utilized. A laser

source at the frequency and linewidth ($\sim 100\,\text{kHz}$) of the master and power of the slave ($\sim 80\,\text{mW}$) is thus obtained.

The slave should be able to follow the injected frequency. This is the case when the frequency of free running diode is in the same region as the frequency injected. This requires temperature and current stabilization of the slave laser.

Chapter 3

Spectroscopy

3.1 Frequency locking

In the previous chapter the need for an absolute frequency measure has been posed. Atomic transitions are fundamental and accurate references to determine frequency characteristics of light. A sample of atoms will absorb light if the frequency of the light as seen by the atoms corresponds to the energy difference between two levels according to,

$$\Delta E = \hbar\omega. \tag{3.1}$$

The absorption will be reduced if the light is detuned from this transition. An absorption profile can be obtained by scanning the frequency of the light entering for example a gaseous sample.

Generally, frequency stabilizing ('frequency *locking*') works by electronically adjusting the frequency if it is detected to be off-resonant. The derivative of an absorption profile becomes negative if the frequency is off to one side and positive if it is off to the other side. Thus one can correct the frequency by feedback of this signal. Different methods how to obtain the derivative will be explained in paragraph 3.2.1.

3.1.1 Atomic spectra

Line broadening

An atomic level has a certain distinct energy. If a transition occurs between two levels the energy difference between these levels corresponds with an exact frequency according to (3.1) . This is the frequency of a photon emitted or absorbed by an atom undergoing this transition. However, there is also a probability that light detuned from this resonant frequency is absorbed or emitted. This results in a *line profile*. Different processes influence the width and the shape of the line profile. These effects are called *line broadening* and can be divided into two groups: homogeneous and inhomogeneous broadening.

Homogeneous broadening implies that all atoms in a certain state have equal probabilities for the broadening effects to occur. For inhomogeneous broadening different broadening probabilities are assigned to different atom classes.

The most important homogeneous broadening of interest here is natural line broadening. The natural line broadening is given by the lifetime of the excited level $\Gamma = 2/\tau$, with τ the lifetime of the excited state. The quantity Γ is known as the *natural linewidth*. In this report Γ will denote the *full* linewidth[1]. Since the lifetimes of the excited states are equal for all atoms in free space, natural line broadening is a form of homogeneous broadening. It can be shown that natural line broadening has a normalized Lorentzian profile [9]:

$$L(\omega) = \frac{1}{2\pi} \frac{\Gamma}{(\omega_0 - \omega)^2 + \Gamma^2/4}. \tag{3.2}$$

The most important inhomogeneous broadening in our case is Doppler broadening. It is based on the velocity spread of the atoms. If an atom is moving with velocity v with respect to the beam propagation the frequency seen by the atom is shifted according to,

$$\omega' = \omega(1 - \frac{v}{c}), \tag{3.3}$$

where ω' is the frequency seen by the moving atom, ω the laser frequency, v the velocity component of the atom in the propagation direction of the beam and c the speed of light. Since the velocity is not equal for all atoms the probability to absorb light of angular frequency ω is not equal for all atoms, hence Doppler broadening is a form of inhomogeneous broadening.

To obtain a high accuracy in frequency stabilization one needs to be able to distinguish between closely spaced transitions which can be obscured by Doppler broadening. Experimental methods to achieve this are pointed out in paragraph 3.2.1.

Line intensities

The shape of a total atomic spectrum is determined by the shapes of the individual lines but also by the line spacings and detection intensities. The line spacings are directly calculated by formula (3.1) . Line intensities have to be derived from relative transition probabilities. These probabilities can be calculated directly from the Clebsch Gordan coefficients associated with the atomic transitions.

One should note that the transition probabilities depend on the polarization of the light used. Light which is $\sigma\pm$-polarized can only drive transitions with $\Delta m_F = \pm 1$, with Δm_F the difference between the quantum numbers of the

---

[1]Generally Γ is used to describe the linewidth of a transition. However, the exact definition varies between Γ being the full or half linewidth. In this thesis Γ describing a linewidth will always correspond to the *full* linewidth.

ground and exited Zeeman sublevel. Light which is π-polarized can only drive transitions with $\Delta m_F = 0$.

Calculated spectrum

In this paragraph a theoretical spectrum will be calculated for ^{87}Rb. The broadening effects described above have been included.

We treat the absorption of a beam of monochromatic light passing through a gaseous sample of ^{87}Rbatoms. The atoms are thermally distributed, therefore the velocity of the atoms is given by the Maxwell velocity distribution [10]

$$P(v) = 4\pi \left(\frac{m}{2\pi k_B T} \right)^{3/2} v^2 e^{-\frac{mv^2}{2k_B T}}, \qquad (3.4)$$

where $P(v)$ is the probability to find an atom with velocity v, m is the mass of the atom, k_B is the Boltzmann constant and T is the temperature of the gas. From this relation and (3.3) one can derive the broadening of a spectral absorption line:

$$I(\omega) = I_0 \left[1 - e^{-\left(\frac{c(\omega - \omega_0)}{\omega_0 v_{mp}} \right)^2} \right] \qquad (3.5)$$

where $I(\omega)$ is the intensity transmitted at angular frequency ω, c is the speed of light, ω_0 is the resonant frequency corresponding to the atomic transition and v_{mp} the most probable velocity given by $v_{mp} = \sqrt{2k_B T/m}$. The broadening has a Gaussian profile with fullwidth:

$$\Delta \omega_D = 4\sqrt{ln2}\,\omega_0 v_{mp}/c. \qquad (3.6)$$

If we apply this to ^{87}Rbwe find that the halfwidth of the doppler broadened D_2 line (see Appendix D) at room temperature is $\Delta \omega_D/(2\pi) \simeq 500\,\text{MHz}$. The hyperfine splitting of the lines is of the order of $50\,\text{MHz}$. Therefore the Doppler broadening needs to be suppressed in order to be able to resolve the hyperfine structure.

If we assume the Doppler broadening is suppressed and use the Clebsch-Gordan coefficients we can derive the ^{87}RbD_2 spectrum as seen in figure 3.1. The properties of ^{87}Rbused are described in Appendix D. This figure shows how a spectrum would look like theoretically. However, an experimentally obtained spectrum depends strongly on the experimental measuring method. An number of effect have to be taken into account in a more detailed calculation of the spectrum.

16
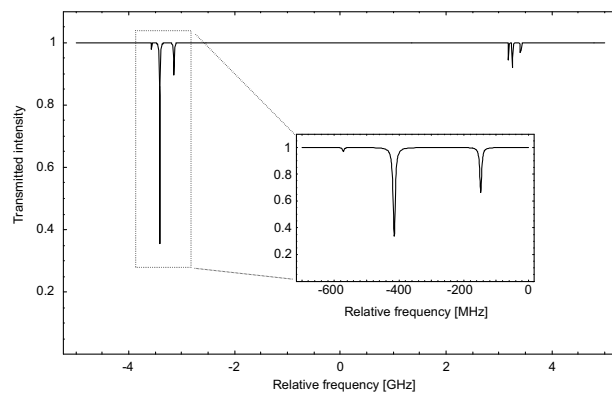
Figure 3.1: *Theoretical example of a spectrum of the $^{87}\mathrm{Rb}D_2$ line. The inset shows a magnification of the transitions from the $F = 2$ goundstate. This spectrum does not include any experimental artifacts. It describes just the line intensities and spacings.*

3.2 Saturation spectroscopy

Saturation spectroscopy is a widely used method to experimentally suppress Doppler broadening. It is based on a selective saturation of an inhomogeneous line profile. The basic concept is as follows. Suppose an intense monochromatic beam with frequency ω is propagated through a gaseous sample and the sample consists of two-level atoms with a resonance frequency ω_0. According to (3.3) the light is absorbed by atoms with velocity,

$$v_a = c \left(\frac{\omega - \omega_0}{\omega} \right). \tag{3.7}$$

The atoms in this velocity class are excited to an upper level. This generates a *Bennet hole*[11] in the ground state population distribution at $v = v_a$ (see figure 3.2a). The hole is of the shape of a Lorentzian. In absence of power broadening it has a width of the natural linewidth of the transition. The depth depends on the intensity of the beam.
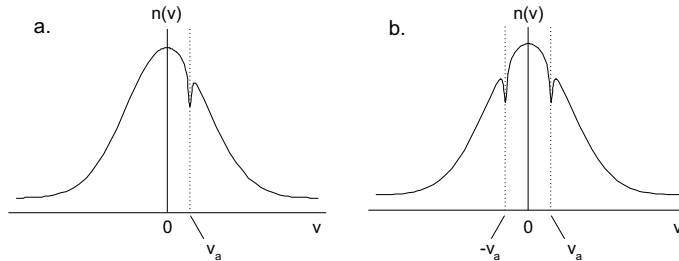
Figure 3.2: *The Bennet hole. Due to the saturation of a Doppler-broadened transition a hole in the number of atoms in the ground state appears. The hole is centered at the velocity class due to the Doppler effect shifted into resonance with the laser frequency. Figure a. shows the number of atoms for only the pump beam. Figure b. includes the counter propagating probe beam.*

3.2.1 Lamb dips

In order to detect the Bennet hole a second beam with the same frequency ω is counter propagated through the sample. One beam (the *pump beam*) generates a Bennet hole for the velocity class: $v = -v_a$ (see figure 3.2b). The absorption of the second beam (the *probe beam*) generates a hole at the velocity class $v = +v_a$. At the frequency $\omega = \omega_0$ the velocity class $v = 0$ is excited by the pump and the probe beam. The pump beam causes a Bennet hole in the velocity class $v = 0$. Therefore less atoms are in the ground state of this velocity class. Therefore the absorption of the probe beam is decreased. This causes a *Lamb dip* in the absorption profile, named after W. Lamb who first described this phenomenon theoretically [12].

The profile is now given by [9],

$$\alpha(\omega) = \alpha_0(\omega) \left[1 - \frac{S_0}{2} \left(1 + \frac{(\Gamma/2)^2}{(\omega - \omega_0)^2 + (\Gamma/2)^2} \right) \right], \qquad (3.8)$$

where $\alpha(\omega)$ is the saturation spectroscopy absorption profile, $\alpha_0(\omega)$ is the Doppler-broadened absorption profile without the pump beam, S_0 the saturation parameter, Γ the natural linewidth. The saturation parameter is given by: $S_0 = \frac{I}{I_{sat}}$, where I is the intensity of the beam and I_{sat} is the saturation intensity [13]. It is clear that the Lamb dip profile is Lorentzian.

(a) (b)
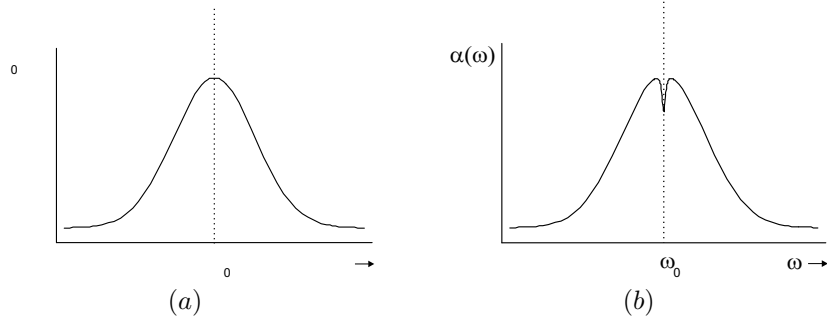
Figure 3.3: Figure a. shows the spectrum of a Doppler broadened transition. Figure b. shows the double passed spectrum. Here a Lamb-dip appears corresponding to the velocity class $v = 0$. The width of this Lamb-dip is determined by the homogeneous broadening factors.

Crossover lines

Now let us look at a three level system with resonance frequencies ω_1 and ω_2 (see figure 3.4) and two counter propagating beams of frequency ω. The spacing of the levels is small compared to the Doppler-width: $\omega_2 - \omega_1 \ll \Delta\omega_D$. Suppose the pump beam interacts with the velocity class $v_c = c(\omega - \omega_1)/\omega$ according to (3.7) . The probe beam acting on the same velocity class is also shifted according to (3.3) :

$$\omega' = \omega \left(1 - \frac{v_c}{c} \right) = 2\omega - \omega_1, \qquad (3.9)$$

with ω' the frequency of the probe beam as seen by the atoms of the selected velocity class v_c. If ω is exactly in between ω_1 and ω_2 equation (3.9) results in

$$\omega' = 2 \left(\frac{\omega_2 + \omega_1}{2} \right) - \omega_1 = \omega_2, \qquad (3.10)$$

i.e. the atoms absorb the probe light on transition 2. Thus the absorption profile also has a dip in between two absorption lines. This is called a *crossover line*.
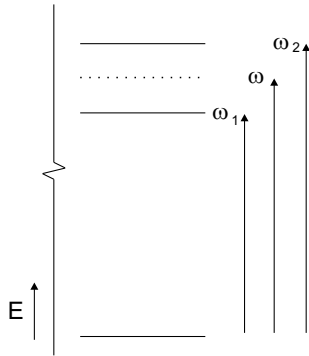
Figure 3.4: *Schematic representation of the energy levels in a three level atom.*
ω_1 *is the angular frequency corresponding to the energy difference between the ground level and the lowest excited level. The angular frequency ω_2 corresponds to the transition from the ground state to the highest excited state. A crossover line appears if the laser frequency ω is exactly in between the two resonant frequencies.*

The above example is called a *V*-crossover transition. Crossover lines can also occur between the hyperfine states of the ground state. These transitions are called Λ-transitions. In our treatment the hyperfine-splitting of the ground state is large as compared to the Doppler profile. Therefore Λ-transitions are not treated.

Dispersive signals

All locking schemes use a dispersive[2] signal to lock on. A dispersive signal can be obtained by modulating the laser frequency. This frequency modulation causes a modulation in the transmitted intensity of the probe beam. The amplitude of the intensity modulation is proportional to: $\frac{d}{d\omega}\alpha(\omega)$. Where a negative $\frac{d}{d\omega}\alpha(\omega)$ implies a phase change of π with respect to the positive $\frac{d}{d\omega}\alpha(\omega)$. The detected signal of the probe beam is multiplied by the sign of the original modulation signal. The phase flip changes the sign of the demodulated signal. The signal also contains a component of twice the modulation frequency around the central frequency. This component is filtered out by the multiplication. Thus a dispersive signal is obtained.

The modulation of the laser frequency can be done by modulating the laser current or by means of an *acousto-optical modulator* (AOM). The advantage of the latter is that only one arm of the setup can be modulated. The disadvantage is that an AOM is rather expensive. Treating this in detail goes beyond the scope of this report. A more detailed description can be found in [9].

---

[2]In this context a dispersive signal is meant to implies a signal anti-symmetric close to the center value.

One obtains an error signal of the locking procedure by measuring the value of the dispersive signal on the locking point. Deviations from zero indicate frequency or electronic fluctuations. This will be used later in this thesis.

Calculations

Calculations of the spectra have been made to obtain insight into the measurements. Nakayama calculated the relative magnitudes of the lines in Doppler-free spectroscopy [14]. His model takes the optical pumping to different Zeeman sublevels into account. The approximation of a single cycle of optical pumping has been made. The former treatment has been applied to ^{87}Rbby Lee et al. [16]. We have compared Nakayama's model and Lee's results with measurements done by us.

Nakayama's model Nakayama's model is based on calculating the electric susceptibility of the atomic system induced by the light. The susceptibility is given by

$$\chi^{(pi)}_{p_j p_j} \sim \sum_{i,j} I^{(pi)}_{p_j p_j} exp\left[-(\Delta\omega_{ij}/2ku)^2\right]/(\omega - \omega_{ij} - i\Gamma), \qquad (3.11)$$

where the pump and probe transitions have frequencies ω_i and ω_j respectively, $\Delta\omega_{ij} = \omega_i - \omega_j$, $\omega_{ij} = (\omega_i + \omega_j)/2$, k is the wave number of the laser light, and Γ is the linewidth of the resonance signal. The sum is over all possible pump (i) and probe (j) transitions. $I^{(pi)}_{p_j p_j}$ is the relative magnitude of the transition with p_i and p_j the polarization states of the pump and probe transitions respectively. $I^{(pi)}_{p_j p_j}$ is obtained from the Clebsch-Gordan coefficients corresponding with ^{87}Rb(see Appendix D).

The absorption coefficient $\alpha^{(pi)}_{p_j p_j}$ is proportional to the imaginary part of the electric susceptibility,

$$\alpha^{(pi)}_{p_j p_j} \sim Im\left[\chi^{(pi)}_{p_j p_j}\right] \qquad (3.12)$$

The absorption spectrum of the ^{87}RbD_2 line is calculated as seen in figure 3.5. For a comparison of the calculated and measured spectra see chapter 5.1.

3.2.2   Zeeman spectroscopy

Zeeman polarization spectroscopy is based on the Zeeman shift of resonance lines due to an applied magnetic field [17]. Furthermore the principle uses the polarization properties of the light.

Linearly polarized light is double-passed through a gaseous sample as explained in section 3.2.1. The atoms can undergo σ^+, σ^- and π transitions by absorbing this light. The $\sigma\pm$ transitions correspond to a change in Zeeman
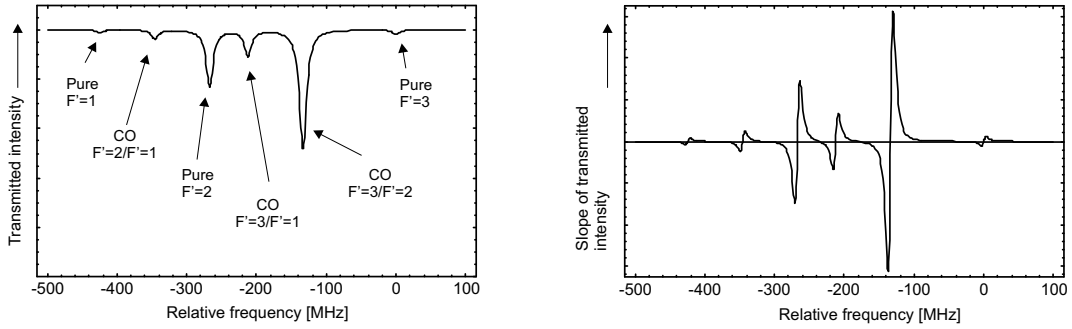
Figure 3.5: *Spectrum as calculated by Nakayama's model. In the figure is indicated which line corresponds with which transition.*

sublevel by $\Delta m_F = \pm 1$. For π transitions the change in Zeeman sublevel is $\Delta m_F = 0$. After its pass through the sample is the probe beam split into its σ^+ and σ^- components. The measured signals of the σ^+ and σ^- absorption profiles are substracted. The contribution of the π transitions to the signal always cancels. In the absence of a magnetic field σ^+ and σ^- transitions are degenerate, therefore their signals cancel.

If a static magnetic field is applied parallel to the beam propagation, the σ^+ and σ^- components experience a Zeeman shift in opposite direction. The magnitude of the shift is proportional to the magnetic field, as will be seen below. If the signals are substracted one obtains a dispersive signal (see figure 3.6). The magnitude of the magnetic field is chosen such that the derivative is constant around zero. The advantage of Zeeman spectroscopy over other methods is that one does not need electronics or modulation to create a dispersive signal. This type of spectroscopy is not sensitive to external magnetic fields. However, large signals have to be substracted, even on resonance. Therefore the stabilization is sensitive to drifts in the gains of the detector and stabilization electronics.
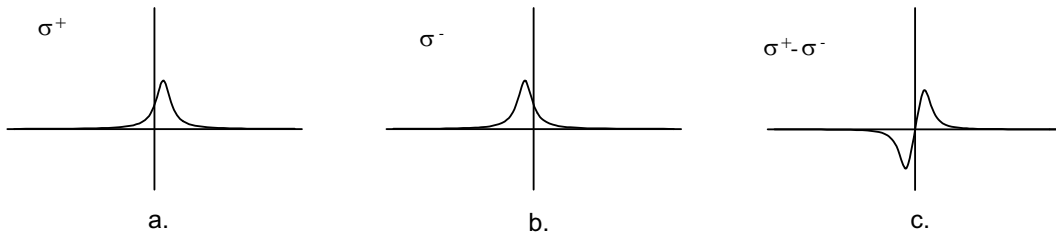
Figure 3.6: *The principle of Zeeman polarization spectroscopy. For all figures the applied magnetic field is pointing along the direction of the laser beam. Figure a and b show the opposite shift of both polarizations. After substraction the signal is as in figure c. On this dispersive signal the laser can be locked.*

3.2.3 Zeeman sideband spectroscopy

Three methods to obtain a dispersive signal have been treated above:

- *Lamb-dip spectroscopy,* a dispersive signal is electronically obtained from an absorption profile.

- *Modulation spectroscopy,* the laser frequency is modulated by means of the laser current or by an AOM.

- *Polarization spectroscopy / Zeeman spectroscopy,* a static magnetic field is applied and the dispersive signal follows from the opposite reactions of the polarizations to the magnetic field.

The first and last methods are quite sensitive to external temperature and magnetic field drifts. The detection in the second method filters low frequency and DC fluctuations out. This is for similar reasons as for the newly developed method as will be explained below. Therefore it is less sensitive to low frequency fluctuations. This is very favorable since drifts (eg. due to temperature) are important problems for long term stability. The disadvantage is that the laser light is modulated in the whole system. By making use of an AOM this can be circumvented, but this is a rather expensive and complex method. Four our purpose long term stability is important. This is because measurements consist of series of measurements over a timespan of hours. The laser has to have the same properties during this time.

In the following a newly developed method will be explained which combines the advantages of all the methods mentioned above. It is a combination of modulation spectroscopy and Zeeman spectroscopy. It will be referred to as *Zeeman sideband spectroscopy.*

Suppose a monochromatic light source propagating through a gaseous sample. The resonance frequency is shifted if a magnetic field is applied. The shift can be expressed by [18],

$$
\begin{aligned}
E_{F,m_F}(B) &= (-1)^F \Big[\frac{1}{2} \hbar \omega_{hf} + m_F g_F \mu_B B \\
&\qquad + \frac{1}{16} \left(4 - m_F^2 \right) \frac{(g_s \mu_B B)^2}{\hbar \omega_{hf}} \Big] + const. \qquad (3.13) \\
g_F &= (-1)^F \frac{1}{2I+1} \, g_s \qquad\qquad\qquad (3.14)
\end{aligned}
$$

where ω_{hf} is the hyperfine splitting of the ground state, μ_B the Bohr magneton, m_F the Zeeman sublevel, g_s the gyromagnetic factor of the electron ($g_S \simeq 2$) and g_F is the total gyromagnetic factor. In the definition of g_F F is the finestate of the atom and I the nuclear spin. This formula is derived in the case of vanishing orbital and nuclear angular momentum, and in weak fields: $g_s \mu_B B \ll \hbar \omega_{hf}$.

The first term describes the hyperfine splitting of the ground state. The second and third term represent the linear and quadratic Zeeman effects respectively. At magnetic fields of the order of $300\,\mathrm{G}$ both contributions are equal. For our purpose the magnetic fields are of the order of $1\,\mathrm{G}$. Therefore we can neglect the 'quadratic Zeeman effect'. By making this assumption the energy of the interaction with the magnetic field is given by:

$$E_{int}(t) = m_F g_F \mu_B B(t) \tag{3.15}$$

Absorption Crossection Let us now analyze what happens to the absorption profile when the magnetic field is fluctuated. In the experiments collimated optical beams are used. These can be treated as plain waves. The intensity of a plain wave through a gaseous sample is given by the Lambert-Beer expression:

$$I_\omega(x) = I_\omega(0) exp[-n\sigma(\omega)x], \tag{3.16}$$

with x the path length of the beam through the sample, n the density and $\sigma(\omega)$ the frequency dependant absorption crossection,

$$\sigma(\omega) = \frac{\pi e^2}{2\epsilon_0 mc} \sum_i \frac{\Gamma/2\pi}{(\omega_i - \omega)^2 + \Gamma^2/4}. \tag{3.17}$$

Here Γ is the natural linewidth of the transitions, assumed to be equal for all transitions, ω_i is the resonance frequency for transition i and the sum is over all possible transitions.

The laser frequency is *only* present in ω and the resonance absorption is *only* present in ω_i. Since the crossection depends on the difference squared, $(\omega_i - \omega)^2$, they can be exchanged. Therefore we can conclude the following: *If the resonance frequency is modulated by an oscillating magnetic field the absorption is the same as if the laser frequency was modulated.* This is even irrespective of any of the atomic properties! Because it is more straightforward *the theoretical treatment will be as if the laser light was modulated.*

Sidebands Suppose the laser frequency is modulated with frequency ω_M. The electro-magnetic field of the laser at time t is given by

$$E(t) = E_0 \sin\left(\omega t + A\sin\omega_M t\right), \tag{3.18}$$

where A is the amplitude of the frequency modulation, given by: $A = \Delta\omega/\omega_M$, $\Delta\omega$ is the maximum deviation of the modulated frequency. This equation can be solved by making use of Bessel functions. The derivation is shown in Appendix A. The result is given by

$$E(t) = E_0 \sum_{n=-\infty}^{\infty} J_n(A)\sin(\omega t + n\omega_M t), \tag{3.19}$$

where, $J_n(A)$ is the Bessel coefficient of order n and argument A [15]. From this equation we see that for a frequency modulated signal *sidebands* appear. The sidebands are located at frequencies: $\omega + n\omega_M$ and have amplitudes $J_n(A)$.

For an amplitude modulated signal given by,

$$E(t) = E_0 \cos \omega t (1 + m \cos \omega_M t) \qquad (3.20)$$

one derives (see Appendix A):

$$E(t) \;\; = \;\; E_0 \left(\cos \omega t + \frac{m}{2} \cos(\omega - \omega_M)t + \frac{m}{2} \cos(\omega + \omega_M)t \right), \quad (3.21)$$

where m is the depth of modulation. The Bessel coefficients for frequency modulation (FM) and the components for amplitude modulation (AM) are shown in figure 3.7a and 3.7b respectively.
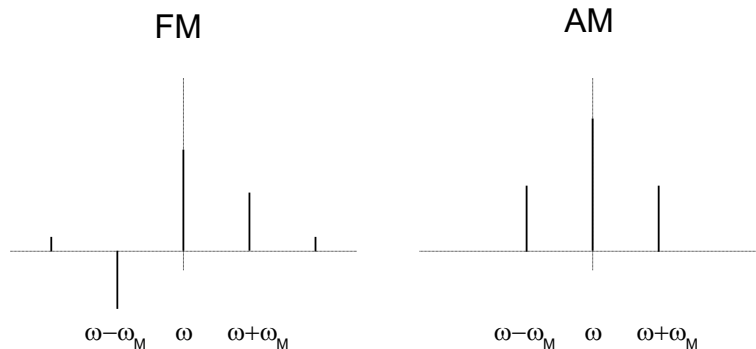
Figure 3.7: *Amplitudes of different frequency components of frequency modulation (FM) and amplitude modulation (AM). The height of the lines indicate the amplitude of the corresponding frequency. Negative amplitudes correspond to signals which have a phase difference of π relative to the positive values.*

The absorption of all frequencies depends on the transfer function of the absorption process. The transfer function is simply the natural line profile. The frequency components of are barely absorbed $\omega + n\omega_M$ for $n \geq 2$. Multiplied by its Bessel function the second order sideband contributes 2% to the total signal. Therefore these frequencies are altered little by the absorption process. They origin from the frequency modulation therefore their contribution to the final signal is also frequency modulation. We are only interested in amplitude modulation as will be explained below. Thus for small detunings these terms are negligible and we will only treat the first order sidebands.

The absorbed signal can be decomposed in a FM and an AM part. The amplitude of the AM part is a function of the detuning and can be described by:

$$S(\delta) \sim J_{-1}(1) \cdot \frac{1}{(\delta + \omega_M)^2 + \Gamma^2/4} + J_1(1) \cdot \frac{1}{(\delta - \omega_M)^2 + \Gamma^2/4} \qquad (3.22)$$

where $\delta = \omega - \omega_0$. If both beams are absorbed by the same amount (the detuning is zero) there is no amplitude modulation component.

The light intensity is measured with a photodiode. The photodiode detects amplitude variations and not frequency variations. Therefore the signal is an oscillating signal of frequency ω_M. The amplitude of the signal on the photodiode is given by the sum of the amplitudes of all sidebands. By demodulating the signal one obtains a dispersive signal of the laserlight.

Optimal modulation frequency   The optimal modulation frequency is expected for the point of maximum response to changes in detuning. From (3.22) we see that this happens when the derivative of the Lorentzian profile (3.2) is maximal

$$\frac{d^2}{d\omega^2} L(\omega) = 0$$

$$\frac{d^2}{d\omega^2} L(\omega) = \frac{\Gamma}{2\pi} \left(\frac{8(\omega - \omega_0)^2}{(\Gamma^2/4 + (\omega - \omega_0)^2)^3} - \frac{2}{(\Gamma^2/4 + (\omega - \omega_0)^2)^2} \right) \quad (3.23)$$

$$\Rightarrow \qquad \omega_{M,optimal} = \frac{\Gamma}{\sqrt{12}} \qquad (3.24)$$

The optimal frequency is expected to be slightly lower. This is due to the fact that the Zeeman state of the atoms is scrambled every time the magnitude of the field is zero. In this process the excited levels are mixed and the saturation decreases. The signal tends to decrease at modulation frequencies of the order of the linewidth. The effect of the scrambling is expected to be small.

Chapter 4

Experiment

4.1 Setup

The design goal of this setup was a highly stable laser with a small linewidth. To obtain this stability the Zeeman sideband spectroscopy as described in the previous chapter is implemented. Furthermore the laser is built on a separate table. This table is placed with a rubber three-point mount in a box. The box has been constructed of aluminium plates to be thermal conductive with the temperature stabilized room. The box isolates the laser from acoustical noise and thermal air flows. The box itself is placed on an air spring to isolate it from vibrations on the ground. It has been shown that the laser stays locked even for very strong vibrations on the ground. Furthermore a low beam height is chosen to achieve higher stability.

Figure 4.1 shows a schematic diagram of the experimental setup used. Both laser diodes are wavelength selected diodes from TOptica (type no. *#LD-0785-0080-1*). The wavelength of the free running diodes is 780 nm. The maximum output power is 80 mW. The laser diodes are mounted in temperature stabilized housings. The master laser is mounted in TOptica model *DL100* which includes the grating and piezo. The slave laser is mounted in a home built housing (see Appendix B for more details). The current and temperature stabilizers used were the *TED 200* (by Profile) and the *LDC 201* (Profile) respectively.
The grating in the *DL100* can scan the wavelength from 776.16 nm to 783.6 nm. An extra mirror has been mounted opposite and connected to the grating. By changing the angle of the grating the output angle of the beam will not change. The optical isolators are to prevent feedback to the laser diodes. The $\lambda/2$ plates are included to set the polarization as needed for the isolators.
The Fabri-Perrot cavity is included to monitor the injection lock and single mode operation. The 90% beam splitter is included because the power required for the spectroscopy is only of the order of 2 mW. The power split off is fed into a fiber coupler for other purposes. Another great advantage of the highly
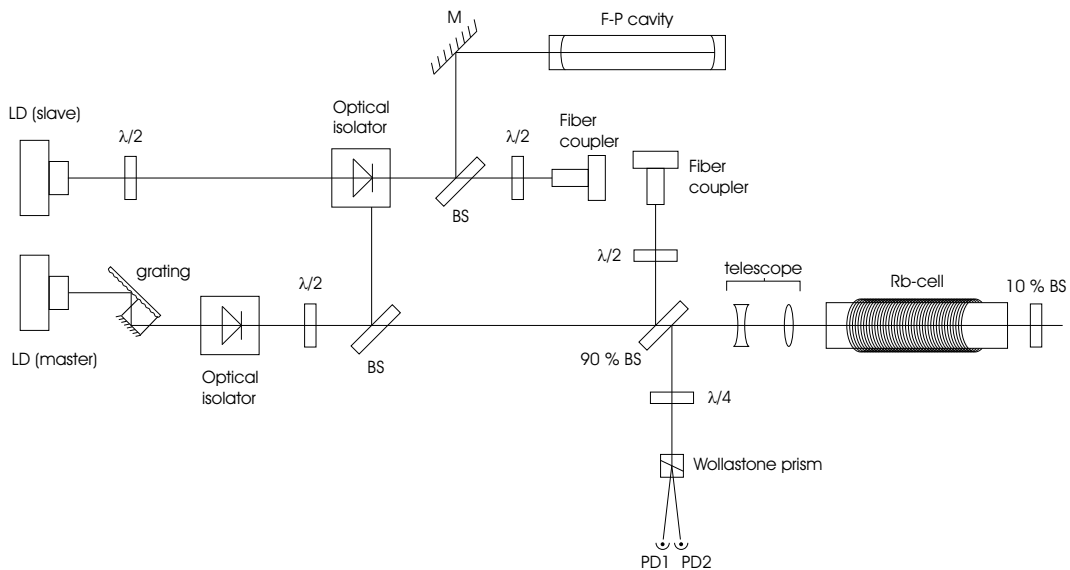
Figure 4.1: *Schematic diagram of the setup of the developed laser. See the text for a detailed explanation.*

reflective beam splitter is that 90% of the probe signal can be detected. The telescope enlarges the beam. The total power in the laser can be bigger without reaching the saturation intensity. This results in a larger signal. The Rb-cell is filled with rubidium vapour and has a coil wound around the tube. The coil can be driven a static current or modulation fields up to the MHz region. The 10% beam splitter makes the probe beam weak compared to the pump beam. The Wollastone prism splits the light into two beams depending on the polarization. In combination with the $\lambda/4$ plate the $\sigma+$ and $\sigma-$ beams are detected separately.

Detector For detection two different setups are used. The non-modulated measurements are done with a single photodiode measuring only one polarization. The Zeeman sideband measurements were done with a high speed detector[1]. A simplified scheme is shown in figure 4.2. The detector consists of two photodiodes which are separately amplified. The contributions of both arms to the total signal is tuned with the variable resistor. The output signal is connected via a transformer to filter the DC component out and subtract the two signals. Both branches are identical. Changes in the environment of the detector will affect both branches in the same manner. Therefore the stability of this setup is by definition better than a non symmetric one.

---

[1]The high speed detector was designed and built by D. Verheijde from the Electronics department of the Amolf institute
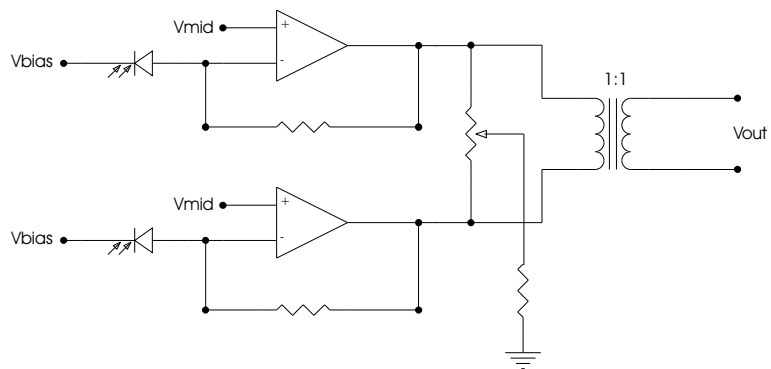
Figure 4.2: *Schematic diagram of the high speed detector. Both amplification branches are identical, therefore any environmental fluctuations will affect both branches in the same manner and cancel at the transformer. This makes the detector less sensitive to the environment. All frequencies below 20 kHz are filtered out. Therefore the detector is also not sensitive to abient light.*

Chapter 5

Results

5.1 Spectra

5.1.1 Saturation spectrum

Figure 5.1a shows the measured absorption profile as explained in paragraph 3.2.1. Figure 5.1b shows the calculated derivative of this data. The measurement was made with a single photodiode measuring the $\sigma+$ polarization. The setup is as shown in figure 4.1. No magnetic field was applied to the absorption cell. In the figure it is indicated which line corresponds to which transition. The crossover lines are much more prominent as compared to the pure lines. This effect can be explained due to the high intensities saturating the sample. Suppose the pump and the probe beam interact with the same transition, generating a pure absorption line. The pump beam saturates this transition. Therefore the probe beam is little absorbed. Consider now the case of a crossover line (as explained in paragraph 3.2.1). In this case the probe beam interacts with a non-saturated transition. Therefore it will be more absorbed as compared to the case of a pure line. In the complete spectrum of the rubidium D_2 line the crossover lines will be more pronounced than the pure lines. These spectra differ from the spectra as calculated in paragraph 3.2.1. This is due to the higher laser power attenuating the pure lines as described above. Also the results by Lee, et al. [16] as stated in paragraph 3.2.1 cannot be compared for the same reason.

5.1.2 Zeeman sideband spectrum

Figure 5.2 shows the same spectrum measured with Zeeman sideband spectroscopy. For this measurement again the setup as shown in figure 4.1 was used. A magnetic field oscillating at a frequency of $238\,\mathrm{kHz}$ with an amplitude of $2.5(2)\,\mathrm{G}$ is applied to the sample.

The optimal modulation frequency was found to be $238\,\mathrm{kHz}$. The signal power could be increased to a frequency of $570\,\mathrm{kHz}$ by making use of a phase
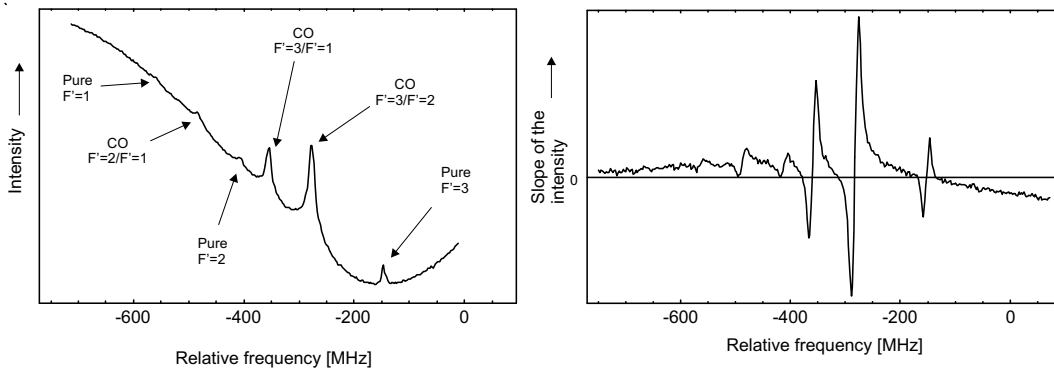
Figure 5.1: *Saturation spectrum of the* ^{87}RbD_2 *line. The spectrum has been measured with a single photodiode detecting only the* $\sigma+$ *beam. No magnetic field was applied to the sample. Figure b. shows the derivative as calculated from this spectrum.*

shifter. However, this increased the signal power little. The signal power can still be increased by optimizing a resonance circuit including the coil.
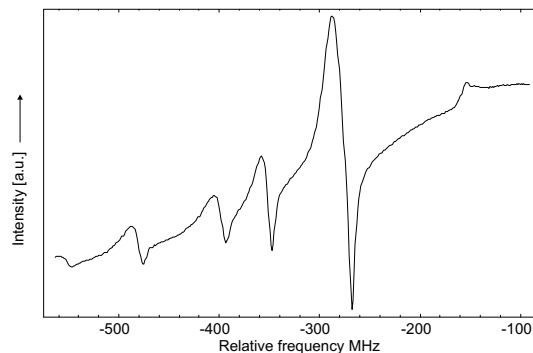
Figure 5.2: *Zeeman sideband spectrum of the* ^{87}RbD_2 *line. The spectrum has been obtained as explained in the text. A magnetic field oscillating with a frequency of* $238\,\text{kHz}$ *with an amplitude of* $2.5(2)\,\text{G}$ *is applied to the sample.*

5.2 Stability

5.2.1 Short/long-term stability

An accurate method to determine the short term frequency stability of a laser is self-homodyne and self-heterodyne detection [19]. These methods are based

on examining only the laser to be characterized. The principle is as follows: the laser beam is split in two branches. One branch is delayed by a fiber. The length of this fiber is at least the length corresponding to the coherence time of the laser. A photodiode is illuminated with the delayed and non-delayed beam. The beams interfere and a beat signal corresponding to the frequency difference is detected by the photodiode. In the self-heterodyne case an AOM is included to shift the laser frequency in one branch. This creates a frequency offset between the two branches, and thus a beat signal at the AOM frequency. This makes it possible to detect the signal with a normal RF spectrum analyzer. In the self-homodyne detection the beat frequency is electronically shifted up to the RF regime. It goes beyond the scope of this thesis to describe the difference in more detail[1]. The disadvantage of this method is that unpractically long fibers are needed (of the order of $100\,\mathrm{m}$) to obtain a bandwidth of the order of $100\,\mathrm{kHz}$. For long term stability even longer fibers are needed.

A more common method is to look at the interference signal of two comparable lasers. Both lasers are locked on different lines. The two lasers are aligned to illuminate one photodiode. The interference of both lasers results in a beat signal. The frequency of this modulation is the frequency difference between the two lasers. By analyzing this beat one can determine the combined stability of the two lasers. If both lasers are identical the individual stability of the lasers is just $1/\sqrt{2}$ of the fluctuation in the beat signal.

The latter method has been used to determine the stability of the laser developed here. The second laser used as a frequency source is the previously used master laser from now on named as *old master*. The newly developed laser will be called the *new master*. As explained above it is only possible to determine the combined stability. The linewidth of the old master has been measured before. Therefore we can get an indication for the linewidth of the new master. This makes this method is applicable.

Short term stability

Both lasers are locked to neighboring lines. The old master is locked by means of unmodulated saturation spectroscopy. The new master by zeeman sideband locking. The old master is locked on the crossover line between the $F = 2 \rightarrow F' = 1$ and the $F = 2 \rightarrow F' = 3$ transitions. The new master is locked on the crossover line between the $F = 2 \rightarrow F' = 2$ and the $F = 2 \rightarrow F' = 3$ transitions. As can be derived from figure D.1 these lines differ by $78.56\,\mathrm{MHz}$ in frequency. The distribution of the noise has been analyzed by measuring the beat-signal with an rf spectrum analyzer. The spectrum is centered around the $78.56\,\mathrm{MHz}$ standard frequency difference. Figure 5.3 shows an example of the spectrum taken. The fit is to a Gaussian (an inverted parabola on a log-scale).

---

[1]Ludvigsen, etc al. [19] has described both methods in detail and compared the results of it.

The agreement of the fit shows that the noise at this detection bandwidth (=resolution bandwidth (RBW)) can be treated as Gaussian.
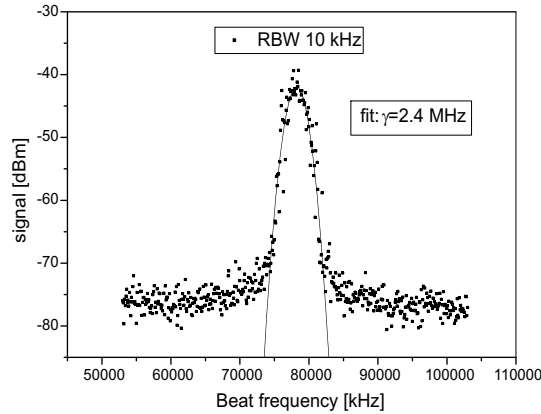
Figure 5.3: *Fit of the spectrum of the beat between two lasers. The fit corresponds to a Gaussian noise distribution. The data points were taken with an RF spectrum analyzer at a detection bandwidth of* 10 kHz. *The measured FWHM is* 2.4 MHz.

The full width at half maximum (FWHM) has been measured for different detection bandwidths. The noise has been observed not to be Gaussian for all detection bandwidths. Therefore a different approach has been used. The FWHM was determined by averaging the data over 10 neighboring points. This is justified because the width of the structure was at least of the order of 30 data points. The full width has been determined at the maximum signal minus 3 dB.

Figure 5.4 shows the FWHM of the measured power spectra as a function of the detection bandwidth. From this plot we can derive most properties of the stability of the laser. Starting from the right hand side of the plot, the measurements are limited by the Fourier transform (1/f) limit of the measurements. This is indicated by the dotted line. At a detection bandwidth of about 50 kHz the noise-distribution is wider than the 1/f-noise only. The detection bandwidth becomes of the order of the fluctuations of the frequency. During one scan the laser center frequency stays constant. At this detection bandwidth the FWHM of the noise distribution indicates the combined linewidth. At lower bandwidths the laser center frequency jitters during the scan. Therefore a broader peaky structure appears. The jitter at $RBW = 30$ kHz has a FWHM of the order of 2.4 MHz.
The spectrum analyzer averages the spectrum over one bandwidth. At even lower bandwidths the jitter stays visible in the spectrum. Therefore the points with a detection bandwidth smaller than 30 kHz (the diamonds) can by prin-

ciple not have a smaller FWHM as the measured 2.4 MHz at $RBW = 30$ kHz. Measurements at lower detection bandwidths are performed in a different manner. This is explained in the next paragraph.

From the data at $RBW = 50$ kHz we derive the combined FWHM as $650(50)$ kHz. If we assume both lasers are identical we derive a full linewidth of $650/\sqrt{2} = 460$ kHz for both lasers. The old master has previously been measured to have a linewidth of < 700 kHz. If we assume the linewidth of the old master is unchanged the new master even has a smaller linewidth. We cannot conclude anything about the separate linewidths of the lasers. However, the found values are narrow linewidths for extended cavity diode lasers.

Long term stability

To examine the long term stability the beat frequency has been measured using a RF counter repeatedly over a period of one measurement day. The measured points have been analyzed for different time-intervals. The FWHM is found by calculating the standard deviation of the fluctuations at a certain detection bandwidth. The FWHM is then given by: FWHM $= 2\sqrt{2\ln 2}\sigma$, with σ the standard deviation of the fluctuations. These points are plotted on the left part of figure 5.4. From this we derive that the stability on an scale of hours is of the order of $100 kHz$. The point at $RBW = 9 \cdot 10^{-5}$ Hz corresponds with a time interval of 3.2 hours. This is typical for the longest continuous BEC measurements done.
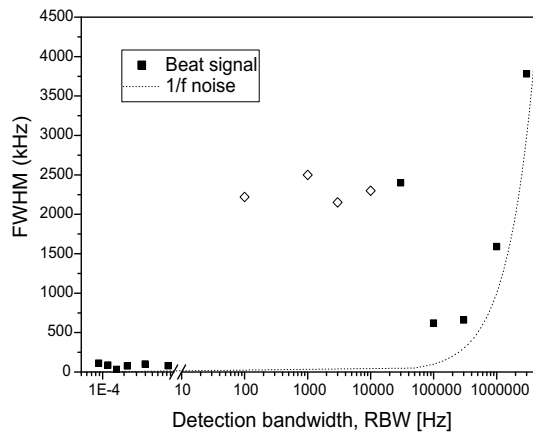
Figure 5.4: *The FWHM of the measured beat spectrum between two lasers. Different bandwidths have been taken to obtain information on the frequency stability on different timescales. The break indicates the difference between measurements done with a RF spectrum analyzer and with a counter. Points left from $RBW = 30$ kHz (the diamonds) have to be interpreted different (see text for explanation). All points are averaged over two samples.*

5.2.2 Environmental stability

The purpose of the laser is to be used in BEC experiments. The old master laser is built on the same optical table as the BEC experiment. For the BEC experiments strong magnetic fields are used. The measurements are generally taken from zero to tens of milliseconds after the magnetic trap has been switched off. The switching off of the magnetic field produces vibrations on the optical table. These vibrations arrive at the old master laser setup about 6 ms after the trap has been switched off. Figure 5.5 shows a typical measurement in BEC experiments. It shows the expansion of a cloud for $0 - 14$ ms in steps of 1 ms after the trap has been switched off. The images are taken with a initial detuning of -15 MHz. It is clear that after 6 ms atoms seem to disappear and appear again. This is due to the detuning of the master laser changes due to the vibrations. For example at 9 ms the frequency is shifted far off resonance, and at 12 ms it is shifted closer to resonance. It has been proven that these pictures are reproducible. However, the fluctuations are on a very fast timescale. Therefore it is not possible to correct for these fluctuations in the measurements. Figure 5.6 shows the number of atoms analyzed from this series of measurements. It is clear that accurate measurements involving the number of atoms after 6 ms of expansion time are impossible.
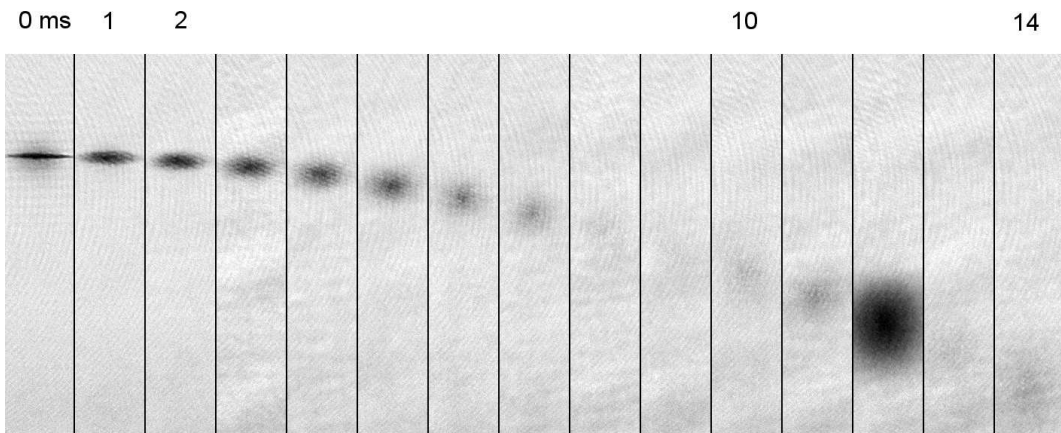
Figure 5.5: *The expansion of a thermal cloud as measured with the old master. The images are taken from* 0 *to* 14 ms *expansion time in steps of* 1 ms. *It is found that the detuning changes in a reproducible manner after* 6 ms *of expansion time.*

In order to isolate the new laser from external vibrations the laser is built on a suspended table. Figure 5.7 shows the error signals of the old and the new master during one of these measurements. The figures are plotted on the same frequency scale. The switching off of the magnetic trap occurs at $t = 0$. At this point a peak in both error signals appear. This is due to an electromag-
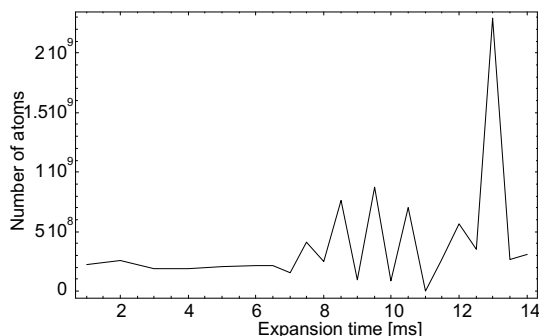
Figure 5.6: *Number of atoms as analyzed from the images seen in figure 5.5. The datapoints have been taken from* 1 *to* 6 ms *in steps of* 1 ms *and from* 6 *to* 14 ms *in steps of* 0.5 ms. *The number of atoms are for each point averaged over two measurements.*

netic pulse generated by the rapid switch off of the magnetic field of the trap. After 6 ms the detuning of the laser starts to make excursions of the order of ± 10 MHz. The new master is not affected by the switching off of the magnetic trap. This makes accurate measurements possible.

One should note that the error signals can be very misleading. One effect is that high frequency fluctuations can be filtered out by the detection electronics. The electronics of the zeeman sideband locking has a frequency cutoff at $f = 2.3$ kHz. The fluctuations as seen in figure 5.7a are of the order of 1 kHz. The oscillation-frequency of these frequency fluctuations are smaller than the bandwidth of the detector and its electronics. Therefore fluctuations of the magnitude as seen in the old master would have been detected in the new master had they occurred. Figure 5.7b shows that these fluctuations are not present on the new master.

A potentially misleading artifact is the conversion of the error signal to a frequency scale. Suppose the detector electronics introduce amplitude variations in the signal. This signal is detected as a frequency variation and hence corrected by the stabilizing electronics. The frequency is now altered such that the detector outputs a signal with minimal fluctuations. This results in little noise on the error signal but can have a big influence on the frequency noise. Therefore these plots can be misleading. For frequency fluctuations one should use the beating measurements as described in section 5.2.1.

The FWHM for the old master as taken from the error signal is found to be: 2.8 MHz (see figure 5.7a [2]). For the new master we find: 0.83 MHz. This results in a combined full linewidth of 2.9 MHz. This value is calculated for the biggest detection bandwidth possible in the error signal measurement ($RBW = 1.7$ kHz). Comparing with figure 5.4 this overestimates the combined linewidth. However, the combined linewidth determined from the error signal is

---

[2]Only the first 20 ms of the data in the figure have been taken into account

only 500 kHz higher than the actual combined linewidth as determined by the beating measurement. Therefore, by judging from the large differences in the error signals it is most likely that the linewidth of the new master is smaller than the linewidth of the old master.

(a)

(b)
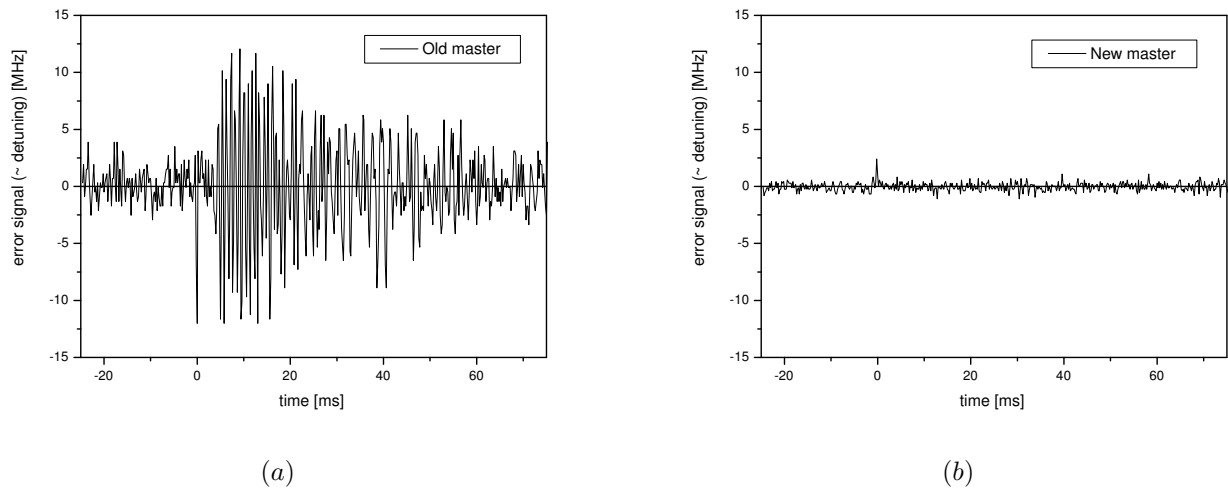
Figure 5.7: *The error signal of the old (figure a) and the new (figure b) master. The vertical scales denotes the frequency difference from the center frequency. Both figures have the same frequency scale. These are derived from the slope of the dispersive signal on the locking frequency. Both error signals have the same amplitudes on a voltage scale. However the locking slope of the new master is much more steep.*

Chapter 6

Conclusion

We can conclude this work in two parts. A new type of spectrometer has been developed. Compared to known types of spectrometry the spectrometer is found to be more stable, less sensitive to external magnetic fields and any DC-drifts and very cost effective. By making use of this spectroscopy a very stable and narrow linewidth laser has been built. It has widened the possibilities of the Bose Einstein Condensation experiments at the Amolf institute. Accurate and highly reproducible measurements over a timespan of hours can now be realized.

Part II

TOP

Chapter 7

Introduction

As seen in the general introduction high phase space densities are mandatory to achieve Bose Einstein Condensation in dilute alkali gases. Magnetic traps provide the tight confinement needed to obtain these densities.

7.1 BEC's in magnetic traps

Tight confinements

The potential energy of an atom in a magnetic field is given by:

$$E = -\boldsymbol{\mu} \cdot \mathbf{B}, \tag{7.1}$$

with $\boldsymbol{\mu}$ the magnetic moment of the atom, given by: $\boldsymbol{\mu} = m_F g_F \mu_B \hat{\mathbf{F}}$, m_F the Zeeman state of the atom, g_F the gyromagnetic factor and $\hat{\mathbf{F}}$ the unit vector in the direction of the total angular momentum.

If we assume that the atoms are magnetically polarized, the potential energy is proportional to the absolute value of the field. In this case tight confinement can be obtained by a gradient in the magnetic field. This results in a V-shaped potential. However, the atoms only stay polarized if the change in magnetic field is smaller than the Larmor frequency. The Larmor frequency is given by:

$$\omega_L = \gamma B, \tag{7.2}$$

$$\gamma = \frac{m_F g_F \mu_B}{\hbar}, \tag{7.3}$$

with B the magnitude of the external magnetic field. The atoms will move in the trapping potential. Therefore the atoms will undergo transitions to other Zeeman sublevels if it approaches the point where B is zero. This change in sublevel can leave the atom in an untrapped state. The atom will be removed from the trap. This process is called *Majorana loss*. Therefore the trapping

potential should not have points in the vicinity of the atoms where the magnetic field is zero.

Ioffe-Quadrupole traps

In Ioffe-Pritchard type of traps a dipole field is added orthogonal to a two dimensional quadrupole field. The magnetic field has always at least the magnitude of the minimum of the dipole field. The total field minimum appears on the point where also the quadrupole field is zero. The axial confinement is generally smaller than the radial confinement. Ioffe-Quadrupole traps have a cylindrical symmetry and result in cigar-shaped condensates. This will be explained in more detail in paragraph 8.1.1.

Time Orbiting Potentials

Another method to achieve no zero field points is by making use of a Time Orbiting Potential (TOP) [21]. This makes use of only a quadrupole field in three dimensions. However, a rotating bias field is added. The field is changed on a timescale fast compared to one over the trapping frequency. Therefore the atoms cannot follow the change in potential. The atoms will see a time averaged potential (see figure 7.1). If the changing frequency of the trapping potential approaches the Larmor frequency the atoms can undergo spin flips to untrapped Zeeman states. Thus the Larmor frequency is the upper limit of the potential changing frequency.

7.2   This project

The Bose Einstein Condensation setup at the Amolf institute uses a Ioffe-Pritchard type of trap. We have developed a model of the trap to examine all possibilities of manipulating the magnetic field. Previous treatments of the Ioffe-Pritchard trap were done analytically. These models rely on symmetry assumptions which are broken for non-symmetric current flows. Therefore a model based on numerical calculations has been made. One should use an analytical model to characterize an abstract trap or to develop a non existing trap. But in the case of an existing trap one wants to know all possibilities. For this purpose a model as explained below is favorable. Furthermore a new method has been developed to apply time averaging potentials in the Ioffe-Pritchard trap. This method opens a wide range of experiments. The details and derivation will be explained in the following paragraphs.
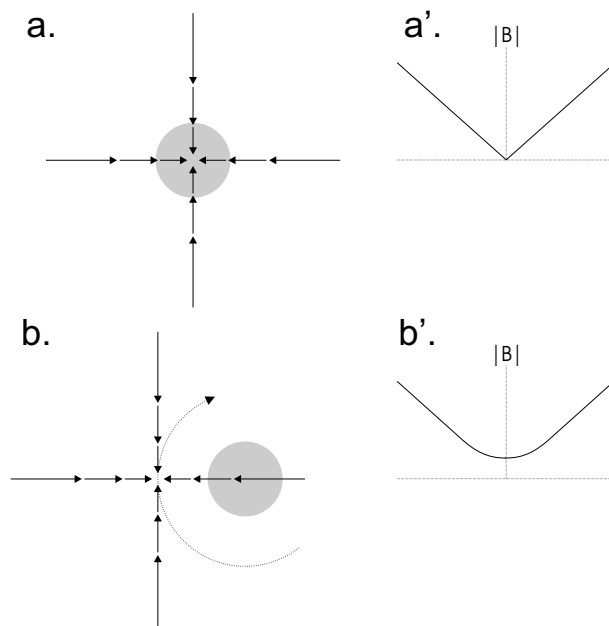
Figure 7.1: *Schematic drawing of the Time Orbiting Potential (TOP) trap. Figure a. and a'. show the stable trap. The cloud (denoted by the grey circle) is in the center of the quadrupole field. Figure b. and b'. show the TOP. The center of the quadrupole field is rotated around the cloud center. The averaged potential in radial direction is as in figure b'.*

Chapter 8

Setup

8.1 Magnetic Trap Model

8.1.1 Introduction

Part of the research project of the quantum gases group at the Amolf institute is to examine oscillations of Bose Einstein Condensates. To excite an oscillation in a condensate the trapping potential needs to be modulated. For this purpose extra coils are mounted next to the Ioffe trap (from now on named as *helper coils*, see figure 8.2). In this chapter will be derived how the trapping potential behaves as a function of the currents through all the coils.

A Ioffe-Pritchard [22] trap consists of four 'racetrack' shaped coils with the centers on the x- and y-axes. These coils are called the *Ioffe-coils*. Two pairs of circular coils are placed on the z-axis as seen in figure 8.1. The magnetic field around the trap center of a Ioffe quadrupole (IQ) trap can be represented in cylindrical coordinates by: [23]

$$
\begin{aligned}
B_\rho(\rho, \phi, z) &= -\alpha\rho\sin(2\phi) - \frac{1}{2}\beta\rho z, & (8.1) \\
B_\phi(\rho, \phi, z) &= -\alpha\rho\cos(2\phi), & (8.2) \\
B_z(\rho, \phi, z) &= B_0 + \frac{1}{2}\beta z^2 - \frac{1}{4}\beta\rho^2, & (8.3) \\
& & (8.4)
\end{aligned}
$$

with α the gradient in radial direction, β the curvature in axial (z) direction and B_0 the magnitude of the magnetic field in the trap center. Around the center of the magnetic field, where $(B(\rho, \phi, z) - B_0)/B_0 \ll 1$, the magnitude of the magnetic field can be approximated by:

$$
B(\rho, z) = B_0 + \frac{1}{2}\left(\frac{\alpha^2}{B_0} - \frac{\beta}{2}\right)\rho^2 + \frac{1}{2}\beta z^2. \tag{8.5}
$$
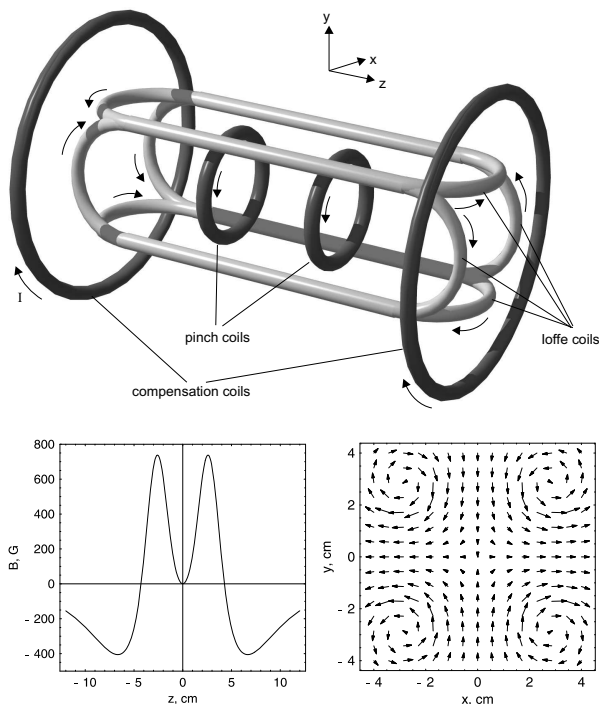
Figure 8.1: *A schematic drawing of the Ioffe quadrupole trap. The bottom left image shows the magnetic field in positive z-direction along the z-axis. The bottom right image shows the radial quadrupole field confining in radial direction. The arrows in the upper figure indicate the flowing direction of the current.*

The current flows as shown in figure 8.1. The setup is symmetric with respect to the center point, with the currents flowing antisymmetric. Therefore the magnitude of the magnetic field is zero in the center. For the current flowing as in figure 8.1 it can be shown that the contributions of the *endcaps* (the loops at the end of the Ioffe coils) cancel in the center of the trap. Therefore this derivation is based upon infinite long rods.

The helper coils are mounted in a similar configuration as the main coils (see figure 8.2). The currents of the helper coils are controlled independently. Therefore the contributions of the endcaps to the field do not cancel by definition. The formulae (8.5) and (8.4) cannot be applied for these coils, and this configuration cannot be solved analytically. However, our aim is to have a tool to gain insight in the trap shape as a function of the applied currents. Thus an model based on numerical calculations also suffices.

The approach to obtain a good, flexible model is as follows. A numerical calculation is made of the field produced by one coil. The obtained data points
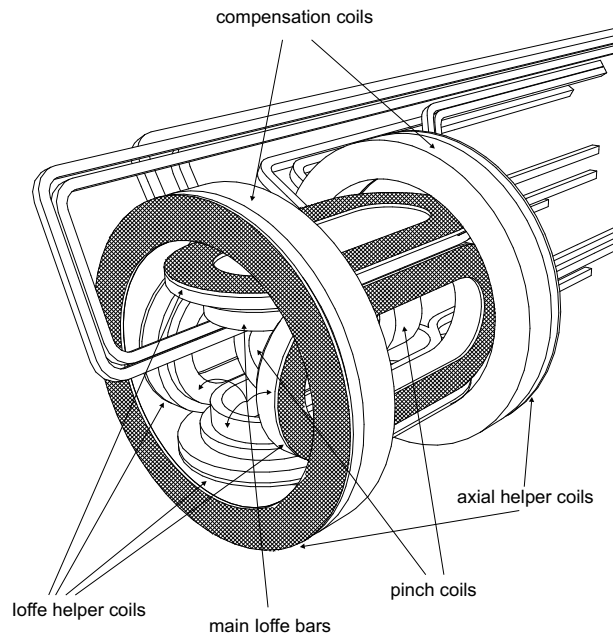
Figure 8.2: *A part of the technical drawing of the magnetic trap used. The coils are denoted in the figure. The arched coils are the helper coils.*

are fitted to an appropriate function. The magnetic field is proportional to the current. Therefore calculating the field for one current through the coil makes it trivial to formulate a function for the magnetic field as a function of the current. This procedure is done for all coils separately. By adding these components one obtains an expression for the total magnetic field as a function of the currents through all separate coils.

The fitted function is a polynomial since the magnetic field of a wire loop theoretically behaves as a power law [20]. The data points are fitted to a polynomial with only the appropriate terms. The selection criteria for these terms are explained in paragraph 8.1.4.

This method seems very crude. However, it provides a semi-analytical model describing the trapping potential very accurately. The model is capable of a very fast calculation of the potential as a function of any current through any of the nine coils. This provides a powerful tool to use next to the experiments.

Three different regions are of interest. Therefore this procedure has been followed three times. The examined regions are:

- *Magneto Optical Trapping stage*, the model is calculated over a region of $2 \times 2 \times 2$ cm.

45

- *The compressed cloud stage*, the model is calculated over a region of $1 \times 1 \times 10$ mm.

- *The condensate stage*, the model is calculated over a region of $10 \times 10 \times 100$ μm.

These three regions have been treated separately to have an applicable model to all stages.

8.1.2 Model derivation

Figure 8.2a and 8.2b show the coils involved in the magnetic trap. The coils shown are:

- *Ioffe coils*, to create the quadrupole field in the xy-plane. This field provides the radial confinement.

- *Pinch coils*, to create the trapping potential in axial direction.

- *Compensation coils*, to compensate for the B-field in the center created by the pinch coils

- *Ioffe helper coils*, to manipulate the quadrupole field.

- *Ioffe axial coils*, to manipulate the axial field.

- *RF-coils*, for the Radio Frequency field to do the evaporative cooling.

- *Earth field compensation coils (not drawn)*, to compensate for the earth magnetic field. These coils are also used to create the B_0.

The earth field compensation coils are located on a large distance from the trap, and therefore not drawn. The degrees of freedom in this setup are the currents through the coils and the frequency of the RF-coil.

8.1.3 Numerical calculation

In this and the following section only the Ioffe-helper coils will be treated. The same procedure has been followed for the other coils.

Figure 8.3 shows a Ioffe-helper coil. It is made of two thin layers of copper. The calculation has been made by integrating the field produced by an infinite thin wire over the region of the copper.

The field of a infinitely thin wire carrying a steady current I is given by the Biot-Savart law [20]

$$\mathbf{B}(\mathbf{r}) = \frac{\mu_0}{4\pi} I \int \frac{d\mathbf{l}' \times \mathbf{r}}{r^3}, \qquad (8.6)$$
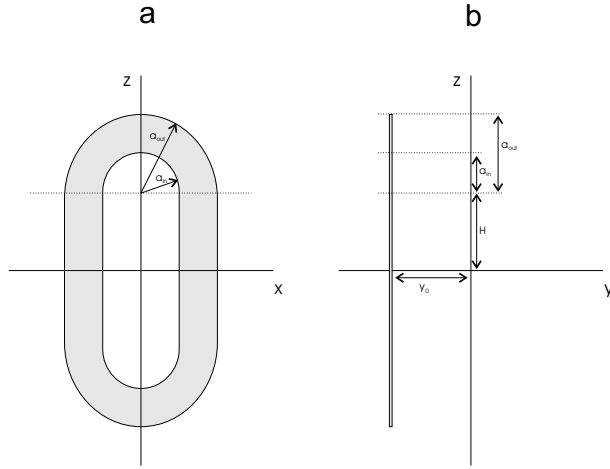
Figure 8.3: *A schematic drawing of a Ioffe-helper coil. The measures are used in the numerical calculation of the field.*

where the integration is evaluated over the wire. For the Ioffe-helper coil the integral is evaluated in two separate parts: one for a half loop and one for a straight wire (from now on named as a *rod*) of finite length. One obtains the contributions of the second curvature and rod by making a rotation around the y-axis. The total magnetic field of the Ioffe-helper coil is then given by:

$$
\begin{aligned}
\mathbf{B}(x,y,z) \quad &= 2 \left(\begin{array}{c} B_{curv,x}(x,y,z) - B_{curv,x}(-x,y,-z) \\ B_{curv,y}(x,y,z) + B_{curv,y}(-x,y,-z) \\ B_{curv,z}(x,y,z) - B_{curv,z}(-x,y,-z) \end{array} \right) \\
&+2 \left(\begin{array}{c} B_{rod,x}(x,y,z) - B_{rod,x}(-x,y,-z) \\ B_{rod,y}(x,y,z) + B_{rod,y}(-x,y,-z) \\ B_{rod,z}(x,y,z) - B_{rod,z}(-x,y,-z) \end{array} \right),
\end{aligned} \qquad (8.7)
$$

where the factor 2 appears for the two windings of the coil. The current distribution through the wire is assumed to be uniform. The two windings are assumed to be on the same point and infinitely thin. This results in two integrals as shown in Appendix C. These integrals have been numerically calculated over the regions stated in paragraph 8.1.1. A resolution of 20 points in all three dimensions has been used. This resolution has been chosen the same for all calculations. The magnetic field of the Ioffe-helper coil is shown in figure 8.4. The coil is located as in figure 8.3 and carries a current of 1 A. This corresponds with a field of 0.113 G in the trap center.

8.1.4 Fitting

The data points are fitted to a polynomial of fourth order in three dimensions. Some terms are zero on symmetry arguments. These are left out in the fitting.
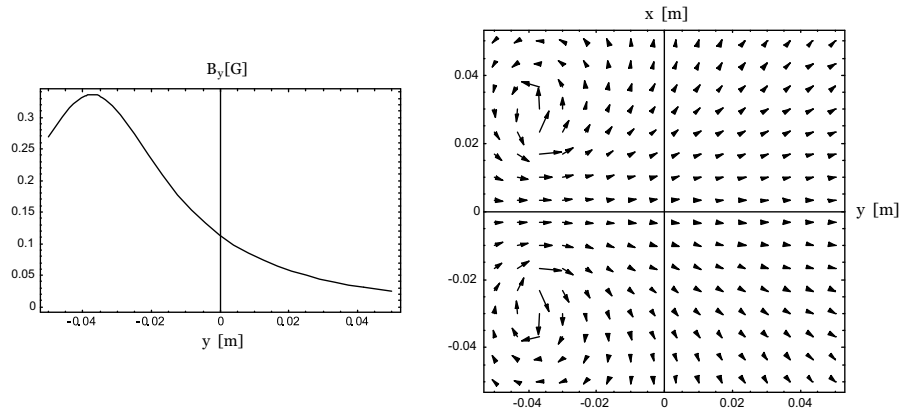
Figure 8.4: *Plots of the magnetic field generated by the Ioffe helper coil placed on the negative y-axis. The left graph shows the magnetic field component in y-direction. These plots are based on the numerical calculation made.*

Figure 8.5 shows three plots of the field components on different axes. For example B_x is an odd function in x, thus all even terms are left out in the fitting. With these nine conditions (all possible combinations of $B_{\{x,y,z\}}$ and $\{x, y, z\}$ the final fitting is done. Fitting to a complete polynomial resulted in negligible coefficients associated with these terms.
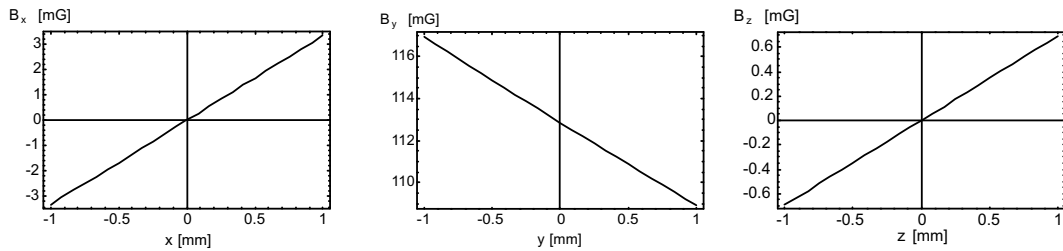
Figure 8.5: *The magnetic field components along different axes. According to such symmetry arguments even or odd terms can be left out in the fitting. See text for more explanation.*

The method used gives an algebraic expression of the magnetic field components around the region of interest as described in section 8.1.1. The coefficients in the expression have no analytical form. However, the coefficients can be easily physically interpreted. For example in a Ioffe-Quadrupole configuration the interpretation of the coefficients appearing in the potential is as follows:

- $0^{th}\ order$, is the offset

- $1^{st}\,order$, is zero since the field is symmetric around the origin of the coordinate system

- $2^{nd}\,order\,radial$ is the harmonic term of the quadrupole part

- $2^{nd}\,order\,axial$, is the curvature of the dipole

- $3^{rd}\,order$, is zero for the same reason as the 1st order

- $4^{th}\,order\,radial$, is the anharmonicity

Accuracy   The accuracy of the numerical calculation is determined by the accuracy of the trap dimensions. The error on the measures is $1\,\text{mm}$. This results in errors in the field of $< 0.5\%$. The error on the fitting procedure is: $< 0.1\%$.

8.2   Model results

8.2.1   Comparison with main Ioffe trap

The model of the Ioffe-helper coils has been verified by integrating the formulae (C.6) and (C.9) over the region of the main Ioffe-coils. The gradient of the resulting field (from four coils) in the center of the trap is compared with experiments. The gradient was numerically calculated to be $362\,\text{G/cm}$ with this model. This differs 2.4% from the measured value ($353\,\text{G/cm}$). The discrepancy may be explained because the Ioffe bars were treated as square racetracks, whereas in reality they are not (see figure 8.2). The endcaps have a more complex form. From this point on the model used for the real trap was a previously made[1] numerical model. This model describes the trap in more detail. The gradient calculated by this model is: $356.5\,\text{G/cm}$, which yields a better agreement with the measured value.

8.2.2   Anharmonicities

Harmonic radius   The region on which the approximation of the potential to a harmonic potential is valid is called the *harmonic radius*. The harmonic radius has been studied in axial and radial direction. A dipole field is created in axial direction by the pinch and compensation coils (see figure 8.1). This is by definition a parabola around the trap center. In figure 8.6a is the correction factor is plotted versus the axial and radial distance from the trap center.

The system is not rotationally symmetric in the xy-plane although the potential is assumed to be. In view of the quadrupole symmetry of the Ioffe bars and the axial symmetry of the dipole field one expects an angular dependance in the potential of the radial harmonic radius. The two most extreme cases are

---

[1]by Robert Spreeuw from the University of Amsterdam

on one of the axes and 45° turned exactly between the x- and y-axis. Both have been calculated by the model and show no difference within the region of interest. Figure 8.6b shows the correction to the harmonic approximation.

The harmonic radius is defined as the radius for which the corrections are 25%. In axial direction the deviation is only 2% over the valid region of our model (see figure 8.6a). In radial direction this is found to be: $43\,\mu$m.
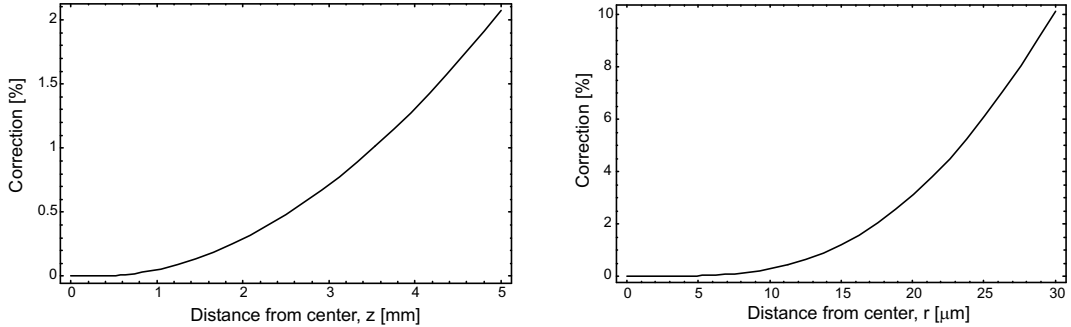
Figure 8.6: *The correction of the real trap to a harmonic trap in both radial and axial direction. It is clear that the axial direction can be much better approximated by a harmonic potential than the radial direction.*

Anharmonic terms   The anharmonicities in axial direction can be neglected as seen in the previous paragraph. The derived field in radial direction (for $z = 0$) is given by:

$$B(r) = B_0 + B_2 \cdot r^2 + B_4 \cdot r^4, \tag{8.8}$$
$$B_0 = 0.89\,[\,\mathrm{G}], \tag{8.9}$$
$$B_2 = 7.13 \cdot 10^8\,[\,\mathrm{G/m^2}], \tag{8.10}$$
$$B_4 = -2.86 \cdot 10^{17}\,[\,\mathrm{G/m^4}], \tag{8.11}$$

The coefficients look big because r is given in meters. The ratio between the fourth order (anharmonic) term and second order (harmonic) term is plotted as a function of r in figure 8.7.

8.2.3   Influence of the endcaps

Generally the endcaps of the racetracks are neglected in theoretical calculations of Ioffe-Pritchard type of traps. This is allowed because most components cancel in the trap center. In the xy-plane the endcaps contribute in the same manner to the quadrupole field as the rods. Here the contributions have been calculated for a thin-wire racetrack of the dimensions centered in our Ioffe-bars located
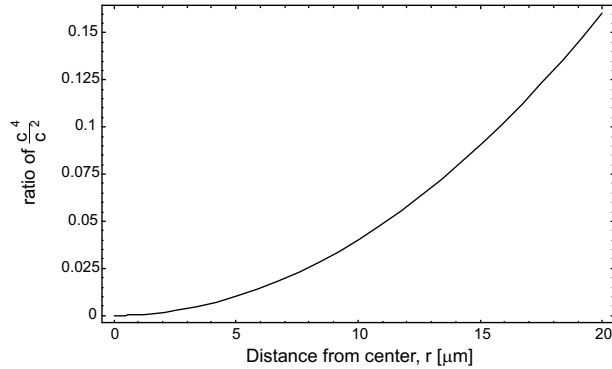
Figure 8.7: *Ratio of the contribution of the anharmonic over the harmonic term. The ratio is plotted as a function of the displacement from the trap in radial direction.*

on the negative y-axis. The contributions of the endcaps to the gradients on the x- and y-axes have been found to be $+6\%$ and $+25\%$ in x- and y-direction respectively.

Z-gradient   Off-axis the endcaps are expected to produce a gradient in z-direction. This can be seen as follows: in figure 8.8a only the contributions of the endcaps to the magnetic field are plotted. The coils will be labelled by its location: $\pm X_0$ for the coils on positive and negative x-axis and $\pm Y_0$ for those located on the y-axis (see figure 8.8b). We also use $X_0 = Y_0$. It is clear that a quadrupole field is produced in the xy-plane and on the z-axis all contributions cancel. Now we look just off the z-axis, for example along $(0, dy, z)$ with dy positive and small compared to all other dimensions. The distance to the centers of the coils at $\pm X_0$ is now: $\sqrt{X_0^2 + dy^2} \simeq X_0$. Therefore the contributions in z-direction of the endcaps at $\pm X_0$ hardly change. However, the distances to the coils located at $\pm Y_0$ is now: $\pm Y_0 + dy$. The contribution from the $\pm X_0$ endcaps together will be bigger than the contribution of the $\pm Y_0$ combined. Therefore, a gradient in z-direction will appear off axis. However, the effect of this gradient has been calculated to be negligible $(17\,\mathrm{mG/m})$.

Tilted endcaps   Another aspect which can affect the trap shape is the method of winding the Ioffe-bars. On one side of the Ioffe-bars the windings of the endcaps are parallel to the x- or y-plane (see figure 8.9a). However, on the other side the windings have to be tilted in order to obtain a coil (see figure 8.9b). The windings of the lower endcap are tilted from down-left to up-right, just as the upper endcap. The components in x and y-directions cancel because the opposite endcaps produce a component in opposite direction.The same applies for the horizontal ones. However, the endcaps create a component in z-direction. This component is the same from the endcap at the other side of the Ioffe bar.

51
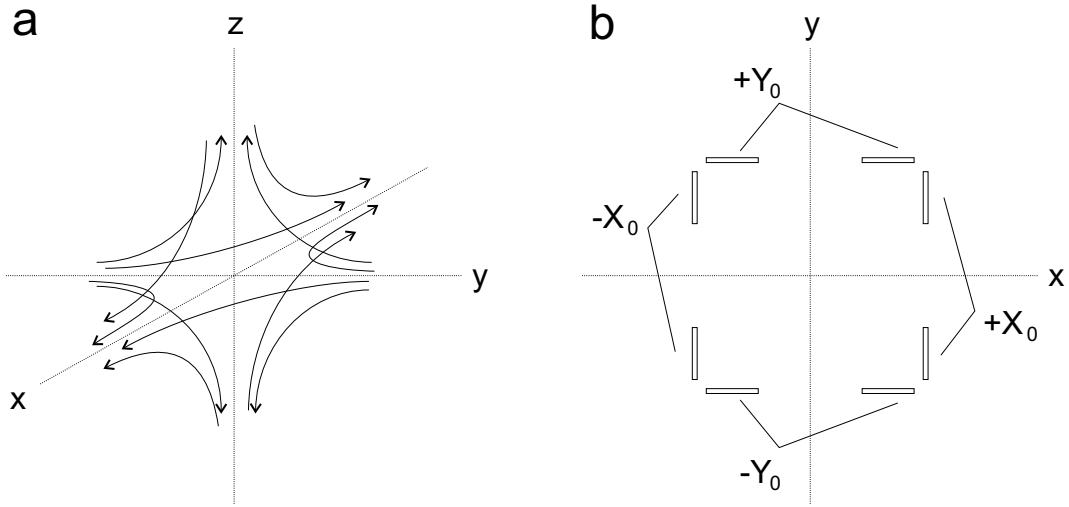
Figure 8.8: *Figure a. shows a three-dimensional representation of directions of the contributions of the endcaps to the magnetic field. The straight section of the helper coils only contribute in the xy-plane. On the x- and y-axis the contributions add up. On the z-axis, the contributions cancel. Off z-axis this leads to a gradient. Figure b. shows the placement of the coils and the denotation of the coils as used in the text.*

However, on the z-axis, the contribution from the horizontal endcap is bigger than the contribution of the tilted one. All four endcap-pairs generate the a z-component of the same size. However, the direction of the horizontal ones is opposite to the contributions of the vertical ones. Therefore no additional field component is created on the z-axis due to this tilt in the endcaps.

Endcaps in our model   The numerical calculation of the main trap assumes infinitely thin endcaps. This assumption can have an influence on the gradient in radial direction. Our calculated gradients in xy-direction will have to be corrected for these effects.

8.2.4   Octopole aspects

The Ioffe helper coils can create an additional homogeneous or quadrupole field as seen above. Suppose the currents are switched such that they run in each rod opposite to the neighboring rods (see figure 8.10a). This creates an octopole field as seen in figure 8.10b. This effect is calculated to be too small to noticeably change the quadrupole aspects of the main field ($< 0.1\%$). Therefore radial octopole excitations are not possible to excite in this manner. The measures indicated in figure 8.10a show the location of rods if the Ioffe helper coils are approximated by thin infinite long rods.
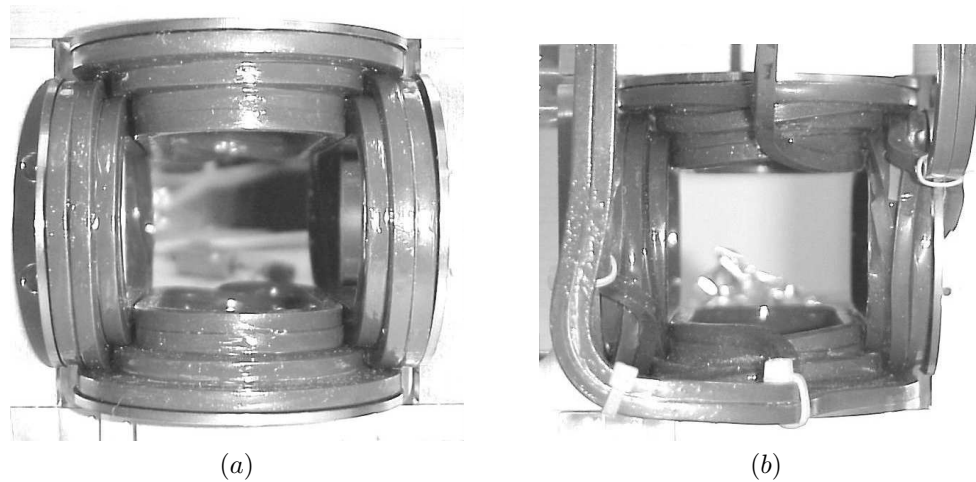
Figure 8.9: *Two photographs of the endcaps of the trap. At one side (figure a) the endcaps are in the same plane as the bars. At the other side (figure b) the windings have to be tilted to obtain a coil. This generates a field component in the z-direction.*

8.3 Dressed trap

The final step in Bose Einstein Condensation is the cooling of the atoms by evaporative cooling. This process is based on selectively removing hot atoms from the trap. It is often compared with blowing away the hot water vapor atoms above a cup of coffee. This removes the hottest atoms and therefore cools the region just above the cup. The coffee rethermalizes by evaporating more atoms. Heat is removed from the coffee and therefore the cup of coffee is cooled. In this process little of the coffee is lost although the cooling is very efficient.

In magnetic traps an electro-magnetic field is used to selectively induce a transition to a different Zeeman state[2]. The untrapped Zeeman states are removed from the trap. For fields used in our case the Zeeman splitting corresponds to frequencies in the Radio-Frequency regime. The potential energy of an atom corresponds to its position in the magnetic field. The RF-field induces a transition to an untrapped Zeeman-shifted energy level of the atom. The highest energy atoms can be removed efficiently by ramping the RF-frequency down.

If one modulates the trapping potential before the evaporative cooling process, the evaporative cooling needs to be taken into account in calculating the

---

[2]The Zeeman state is defined by the m_F quantum number which describes the spin state. Spin state and Zeeman state are both used to describe the state. Their definition is identical.
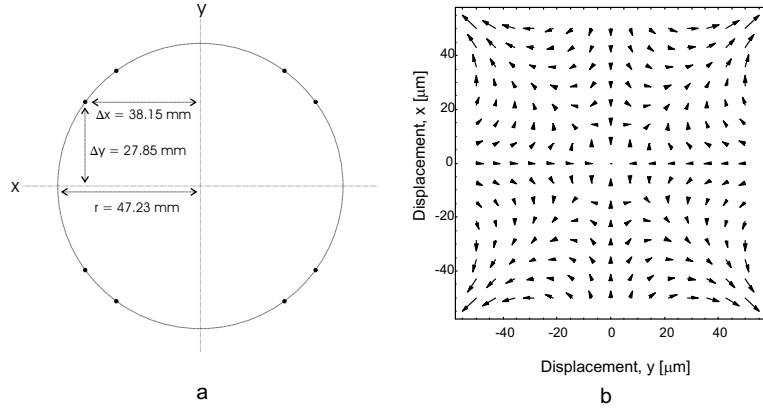
Figure 8.10: *The octopole field as created by the Ioffe helper coils. The currents in every rod runs in opposite direction to the neighboring rods. This generates an octopole field as shown in figure b. The measures denoted in figure a. show the location of the rods if the Ioffe helper coils are approximated by thin wire racetracks.*

magnetic field. Therefore we need to include the evaporation process in our model. A widely used model to describe the evaporative cooling is the dressed trap picture. In this picture the trapping potential is treated to be deformed by the RF-field. The derivation goes as follows.

The equation of motion for a magnetic dipole in a time-dependant field is given by:

$$
\begin{aligned}
\frac{d}{dt}\mathbf{m}(t) &= \gamma \mathbf{m}(t) \times [\mathbf{B}_0 + \mathbf{B}_1(t)], & (8.12) \\
\gamma &= \frac{g_F \mu_B}{\hbar},
\end{aligned}
$$

where $\mathbf{B}_0$ is the static part of the field, $\mathbf{B}_1(t)$ the time-dependant part (in our case the RF-field) and γ the gyromagnetic ratio of the atoms. $\mathbf{B}_1(t)$ is assumed to be perpendicular to $\mathbf{B}_0$ and rotating around it with an angular velocity ω. The components can be written as:

$$
\begin{aligned}
\omega_0 &= -\gamma B_0, & (8.13) \\
\omega_1 &= -\gamma B_1, & (8.14)
\end{aligned}
$$

We can choose our coordinate system such that $\mathbf{B}_0$ points along the positive z-axis. If we now look from a frame rotating with angular frequency ω around the z-axis (the restframe of $B_1(t)$) the magnetic moment becomes:

$$
\left(\frac{d}{dt}\mathbf{m}(t) \right)_{rot} = \frac{d\mathbf{m}}{dt} - \omega \mathbf{e}_z \times \mathbf{m}(t), \qquad (8.15)
$$

54

Using equation (8.12) in (8.15) , one obtains:

$$\left(\frac{d}{dt}\mathbf{m}(t)\right)_{rot} = \mathbf{m}(t) \times [\Delta\omega\mathbf{e}_z - \omega_1\mathbf{e}_x], \qquad (8.16)$$

with $\Delta\omega = (\omega-\omega_0)$. This is the same situation as if the dipole precesses around a static effective field given by:

$$\mathbf{B}_{eff} = \frac{1}{\gamma}[\Delta\omega\mathbf{e}_z - \omega_1\mathbf{e}_x]. \qquad (8.17)$$

If we now describe the potential $(U = \mu \cdot \mathbf{B})$ in the restframe we obtain the so called *dressed potential*:

$$B_{dressed} = m_F\gamma\left(B_1 \pm \frac{1}{\gamma}\sqrt{(\omega - \omega_0)^2 + \omega_1^2}\right), \qquad (8.18)$$

where the plus or minus sign depends on the sign of the Zeeman state of the atom. The minus sign corresponds to low-field seekers and the plus sign to high-field seekers. Here ω is the rotation of the field, in the case of evaporative cooling this is the frequency of the RF-field; ω_1 can be interpreted as the Rabi-frequency of the dressing.

The details of the properties of evaporative cooling process goes beyond the outline of this report. A treatment in greater detail can be found in [24] or [25].

Chapter 9

Applications of the model

Time Orbiting Potentials have been widely used to achieve BEC's in magnetic traps [21]. Generally a gradient is applied in the radial direction and the axial direction. A TOP trap with an adjustable aspect ratio has been reported [26]. This so called *zTOP* oscillates the bias field in three in stead of two dimensions.

In this thesis the application of an ordinary TOP and a newly developed TOP trap will be explained. The former will be called the *Pinch TOP*. The latter principle is based on a Ioffe-Quadrupole trap. The trapping in axial direction is done by a dipolar field. The trapping in radial direction is done by a normal quadrupole field (see figure 9.1a and 9.1b). The quadrupole contribution will be oscillated. Two applications will be treated. First a Double TOP-trap, second a method to obtain an elliptic deformation of the trapping potential in the xy-plane.

9.1 Pinch-TOP

Suppose the direction of the current in one pinch coil is reversed. This configuration will be called *Anti Helmholtz Configuration (AHC)* as opposed to the previous *Helmholtz Configuration (HC)*. The pinch coils now create a gradient in stead of a dipolar field. If the compensation coils are switched off a gradient is present in all directions. This implies a field zero in the trap center. By applying a rotating bias field with the Ioffe helper coils an ordinary TOP is created. The aspect ratio of the trap is proportional to the ratio of the currents through the pinch coils and the Ioffe coils. This system has been calculated by the model.

Aspect ratio's of $\omega_\rho/\omega_z = 1 : 2$ can be achieved in our trap. This implies that this type of trap can realize BEC's with aspect ratio's from $\omega_\rho/\omega_z = 25 : 1$ up to $\omega_\rho/\omega_z = 1 : 2$. Trapping atoms in shallow traps is found to be hard to realize. Therefore experimental realization of these 'pancake' aspect ratio's can be difficult.

9.2 Double TOP

Suppose the offset field is gently decreased to a negative value. Figure 9.1c shows the axial trapping potential. In the process of changing to this negative offset the cloud will be split into two parts. However, in the resulting double trap there is a zero in the magnitude of the field. Therefore the trapped atoms will undergo Majorana losses and the condensate will not be stable. Suppose now the center of the quadrupole field is rotated around the z-axis. The rotating frequency is large compared to the trapping frequency and slow compared to the Larmor frequency. The atoms cannot follow this fast change in potential and see the time average. The potential at an instant time is given by:

$$U(x, y, z, t) = |(x\alpha + B_b \cos \omega_r t)\hat{x} + (y\alpha + B_b \sin \omega_r t)\hat{y} + B_z(x, y, z)\hat{z}| \quad (9.1)$$

where, α is the gradient of the quadrupole field, B_b the magnitude of the rotating field, B_z the field in axial direction and ω_r the angular frequency of the rotating field.

After time-averaging equation (9.1) one obtains for the trapping potential near the z-axis (small r):

$$
\begin{aligned}
U(r, z) &= \sqrt{B(0, z)^2 + B_b^2} + \frac{16\alpha^2}{(B(0, z)^2 + B_b^2)}r^2 & (9.2) \\
r &= \sqrt{x^2 + y^2} & (9.3)
\end{aligned}
$$

From this we see that at points where the axial field B_z vanishes, there is still an offset field created by the bias-field. Therefore the centers of the small wells will also have a non-zero field (see figure 9.1e and 9.1f). The averaged dipole field in z-direction is now given by:

$$U(0, z) = \sqrt{(B_0 + \frac{1}{2}\beta z^2)^2 + B_b^2} \quad (9.4)$$

where β is the curvature of the dipole field. Combining (9.4) and (9.3) we derive:

$$U(r, z) = \sqrt{(B_0 + \frac{1}{2}\beta z^2)^2 + B_b^2} + \frac{16\alpha^2}{(B_0 + \frac{1}{2}\beta z^2)^2 + B_b^2}r^2 \quad (9.5)$$

This rotating field will have a circle where the field is periodically zero. In literature this is called the *circle of death*. This circle should be large compared to the size of the trapped cloud to avoid Majorana losses.

This *Double TOP* provides the trapping potential for two condensates in a completely symmetric manner. As far we know the realization of two condensates in a Ioffe Quadrupole trap by purely magnetic means has never been reported. It opens a wide range of experiments to examine the interaction between to condensates.

9.2.1 Experimental approach

Condensation scheme The experimental scheme to condensate rubidium atoms in the double trap is as follows. The start of the condensation scheme is as explained in the general introduction. The TOP is switched on just before the compression and evaporative cooling stages. The evaporative cooling is performed to a temperature above the critical temperature T_c. The cloud has at this point a size smaller than the radius of the TOP. The offset field is gradually set negative and the cold cloud is split. Finally evaporative cooling is done to cool the cloud below T_c. Figure 9.2 shows a scheme of the condensation process in the Double TOP. In the first 10 seconds the cloud is evaporated to an intermediate frequency of $\nu_{RF,int}$. The temperature of the cloud at this point depends on the B_0 and $\nu_{RF,int}$. The temperature can be calculated by

$$T = \frac{\hbar}{k_B}\Delta\nu = \nu_{RF,int} - \frac{2\pi g_F \mu_B m_F}{k_B}B_0, \tag{9.6}$$

where $\Delta\nu$ is the difference of $\nu_{RF,int}$ and the frequency corresponding to B_0. For the following 2 seconds the RF evaporation frequency is kept constant. During this time the B_0 is ramped to a negative value of B_{split}. This splits the cloud in two. The following 600 ms the B_0 is kept constant and the RF-frequency is ramped down to an end value of $\nu_{RF,end}$. Then the evaporation is kept constant for a time τ_{plain}, the cloud is let to thermalize. Depending on the value of $\nu_{RF,end}$ two cold thermal clouds or two condensates are obtained. Then two time parameters are introduced τ_{hold} and τ_{exp} to hold the cloud in the trap and let it expand respectively. These parameters will be used later on.

Optimal intermediate RF-frequency The splitting of the clouds leads to heating. Therefore it is expected to be most efficient to split the cloud as hot as possible. However, for a negative B_0 the TOP has a circle of death as explained above. Therefore *the size of the cloud should be smaller than this radius whilst being split*. This radius is expected to be the radius to obtain the highest number of atoms in the double trap. From this radius one can calculate the temperature of a cloud which fits in the trap. This will be named the *trap depth*. Figure 9.3 shows the radius and the trap depth of the TOP as a function of the amplitude of the TOP. Figure 9.4a shows the size of the trap as a function of the intermediate evaporation frequency $\nu_{RF,int}$. Figure 9.4b shows the temperature as a function of the intermediate or end evaporation frequency.

The volume of the cloud is changed due to the splitting of the cloud. The change of the volume of the cloud in time is a measure for the heating. The normalized volumes for clouds at different temperatures have been plotted as a function of the field in figure 9.5. All four plots have been calculated by our semi-analytical model described above. From these plots one should determine the optimal evaporation end frequency.

Experimental results are shown in chapter 10.

9.3 Elliptic trap

The quadrupole field can be approximated by a quadratic potential for small values r. The anharmonic terms contributing to the potential are often neglected. However, this anharmonicity can be exploited to obtain different trapping frequencies in $x-$ and $y-$directions.

Suppose the potential in $x-$direction is described by:

$$U(x) = \sqrt{\alpha^2 x^2 + B_0^2} \tag{9.7}$$

where α is the gradient of the trapping field and B_0 is the offset field in axial direction. This potential can be expanded around $x = 0$ as:

$$U(x) = B_0 + \frac{\alpha^2}{2B_0}x^2 - \frac{\alpha^4}{8B_0^3}x^4 + O(x^6) \tag{9.8}$$

Suppose, furthermore, an oscillating homogeneous bias field is applied in the x-direction. This is equivalent to shifting the trap back and forth. The shifting is done fast compared to the trap frequency in radial direction, therefore the atoms see the averaged potential. The average is given by:

$$\bar{U}(x) = \int_{\phi=0}^{2\pi} \sqrt{\alpha^2 + (x + A\sin\phi)^2 + B_0^2} \tag{9.9}$$

$$= \int_{\phi=0}^{2\pi} B_0 + \frac{\alpha^2}{2B_0}(x + A\sin\phi)^2 - \frac{\alpha^4}{8B_0^3}(x + A\sin\phi)^4 \tag{9.10}$$

$$= C_0 + C_2 x^2 - \frac{\pi\alpha^4}{4B_0^3}x^4, \tag{9.11}$$

$$C_2 = \left(\frac{\pi\alpha^2}{B_0} - \frac{3A^2\pi\alpha^4}{4B_0^3}\right) \tag{9.12}$$

where A is the amplitude of the modulation and C_0 the offset of the averaged potential. The harmonic trapping frequency is given by [18]:

$$\omega = \sqrt{\frac{\mu_B g_F m_F}{m} \cdot 2C_2} \tag{9.13}$$

From (9.11) and (9.13) we derive that the trapping frequency in x-direction of the averaged potential is given by:

$$\omega_x = \sqrt{\frac{\mu_B g_F m_F}{m}} \cdot \sqrt{2\left(\frac{\pi\alpha^2}{B_0} - \frac{3A^2\pi\alpha^4}{4B_0^3}\right)} \tag{9.14}$$

From the first term we see that applying a bigger offset field opens the trap (this is the same in y-direction). However, the second term shows that the trap opens as the amplitude of the modulation increases. This modulation in x-direction does not affect the y-direction, therefore this method can be used to generate different trapping frequencies in x- and y-directions. Figure 9.6 shows the ellepticity as a function of the bias field. These plots have been calculated by our semi-analytical model.

This ellipticity in the xy-plane can be used for different purposes:

- *radial quadrupole oscillations.* Driving the amplitude of this asymmetry can excite quadrupole oscillations. Breathing modes (x/y are in phase) and second order quadrupole modes (x/y are out of phase) can be realized.

- *generating vortices.* Different amplitudes of the modulations in x- and y-directions are applied. These amplitudes are given by $\cos\theta$ and $\sin\theta$. An opened trap under an angle of θ is obtained. Changing this θ can stir the condensate around the z-axis. Vortex formation due to stirring a condensate has been demonstrated by Madison, et. al [27]. The stirring was done with a focused laser beam generating differences in radial trapping frequencies of the order of 10%. For a current of 5 A through the helper coils we have an asymmetry in radial direction of 20%[1].

One should note that the trap is only opened in the center. Further outside the region of interest the trapping potential is not changed. Due to the anharmonicities the trap is flattened out in the center. This approximation indicates the presence of an harmonic radius created by this method. A surprising effect is that the harmonic radius *increases* due to this field averaging. The lowering of the trapping frequency and the same asymptote for large r require a more harmonic trap in the center. Figure 9.7c shows the averaged trapping potential in x- and y-directions and the original (non-averaged) trap. Figure 9.7a and 9.7b show the ellipticity for different oscillation amplitudes.

---

[1] Vortex formation by purely magnetic means with an ellipticity in the xy-plane of the same order has been reported by Hodby, et. al [28]. However, this has been achieved by an ordinary TOP where the quadrupole field follows an ellipse around the center in stead of a circle.
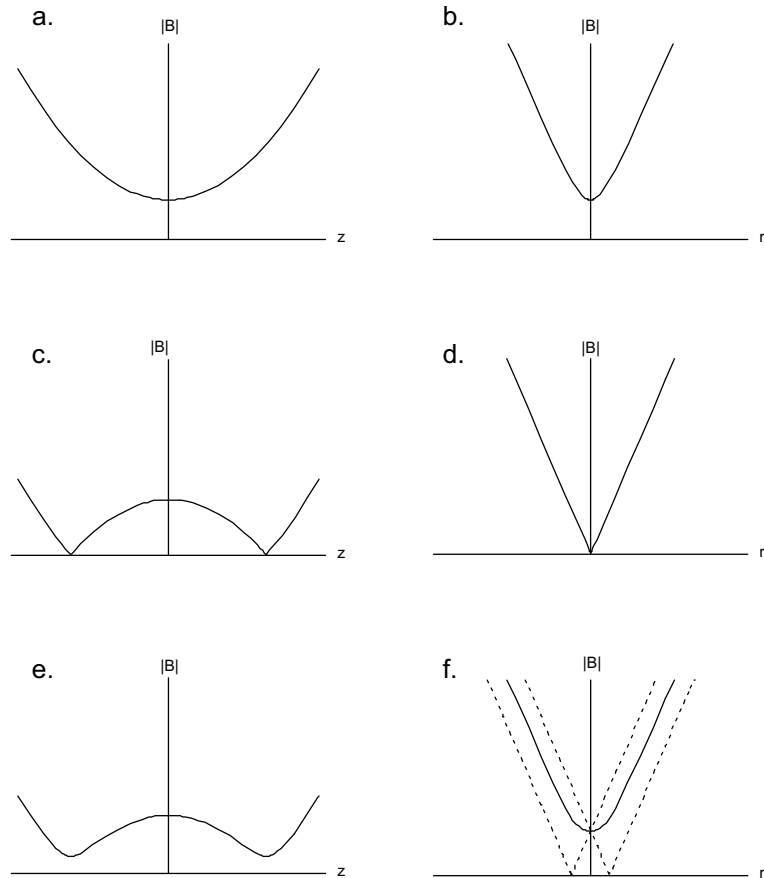
Figure 9.1: *The principle of Time Orbiting Potentials. Figure a. and b. show the magnitude of the field of a normal Ioffe-Quadrupole trap in axial and radial direction respectively. If the external B_0 is lowered below zero the magnitude of the field is as in figure c. and d. Due to the field zeroes high losses of atoms will occur. If the quadrupole field in radial direction is rotated around the z-axis the averaged potential in radial direction will look as in figure f. The dotted lines indicate the instantaneous potential halfway the cycle. This time averaging will create a trapping potential in axial direction as in figure e.*

61
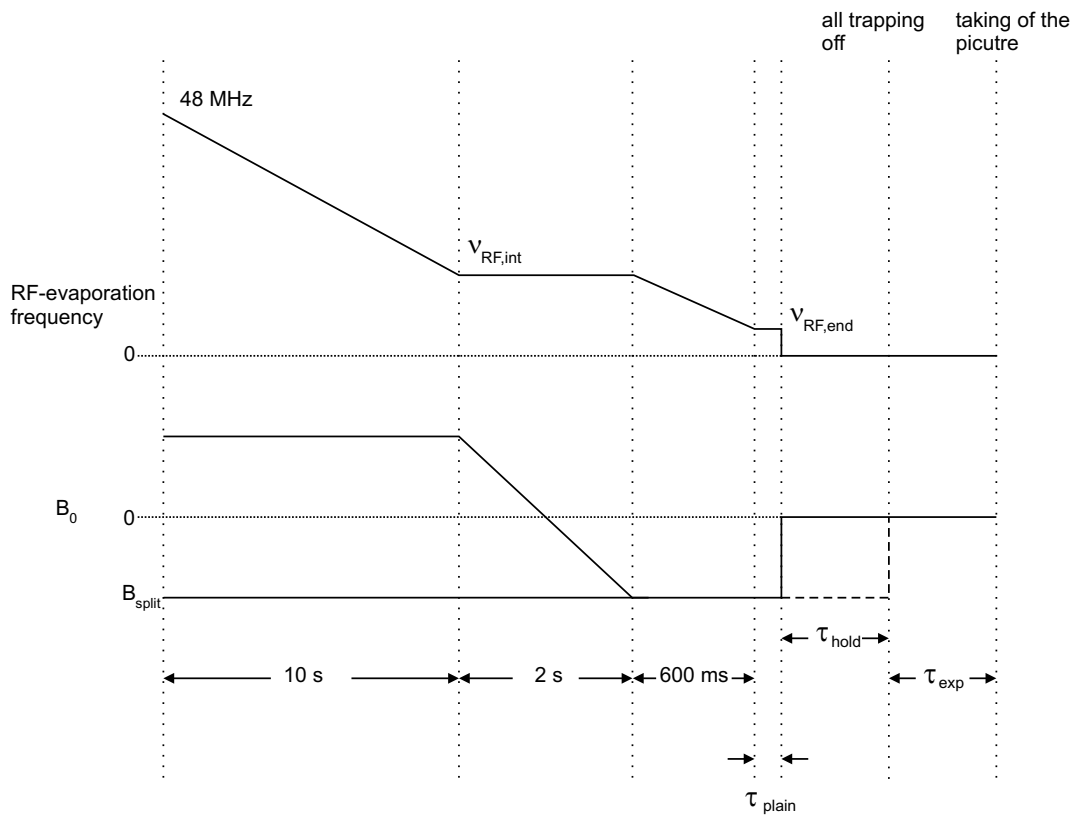
Figure 9.2: *Schematic diagram of the steps to obtain a double condensate. See text for details.*
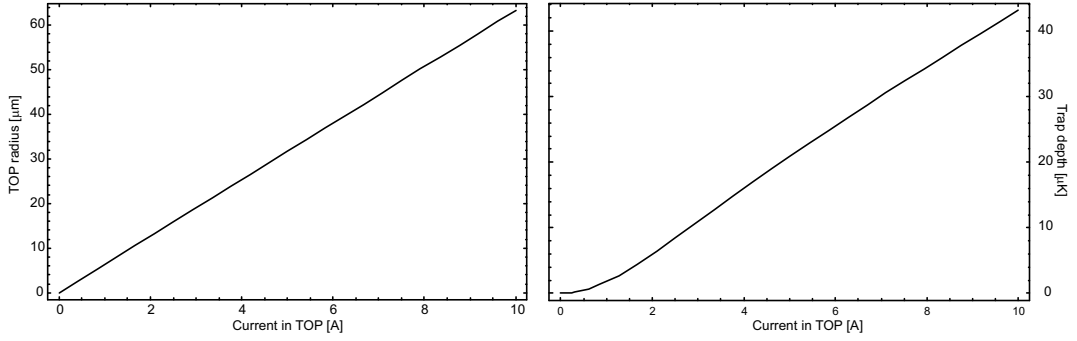
Figure 9.3: *Figure a. shows the radius of the TOP as a function of the current. The linear dependence follows simply from applying an homogeneous field to a pure quadrupole field. This linearly shifts the trap center. Figure b. shows the trap depth in μK as a function of the TOP amplitude. This indicates how hot the cloud maximally can be due to the evaporation by the circle of death in a double TOP.*
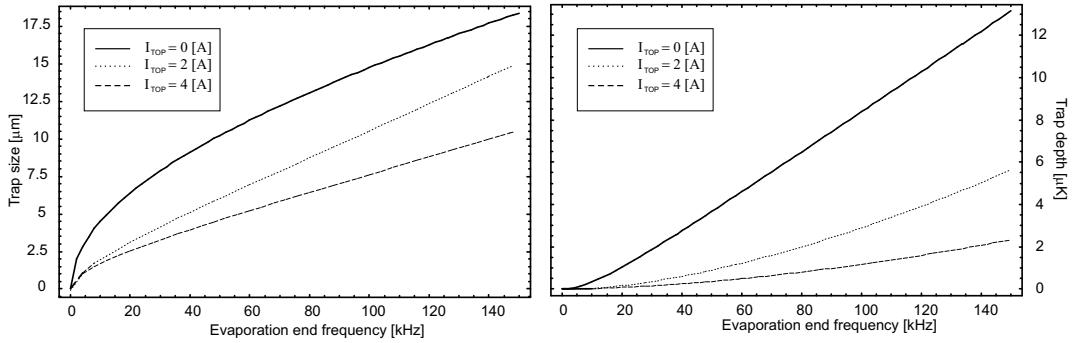
Figure 9.4: *The trap size and temperature as a function of the evaporation end frequency. These calculations include the dressed trap as pointed out in section 8.3.*
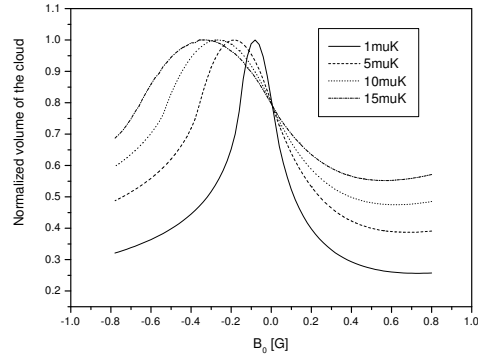
Figure 9.5: *The volume of the trap as a function of the magnetic field. The different plots are for different temperatures (sizes) of the cloud. The plots are normalized for plotting convenience.*
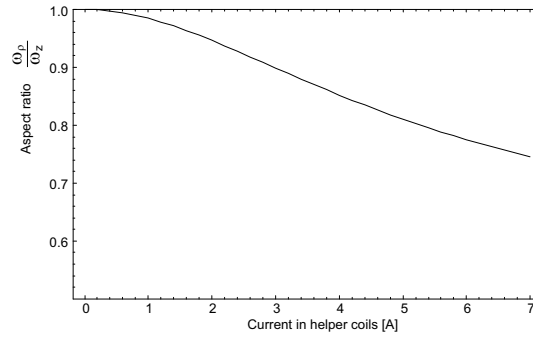
Figure 9.6: *Aspect ratio of the elliptic trap as a function of the current through the Ioffe helper coils. This indicates that strong radial deformations can be obtained.*
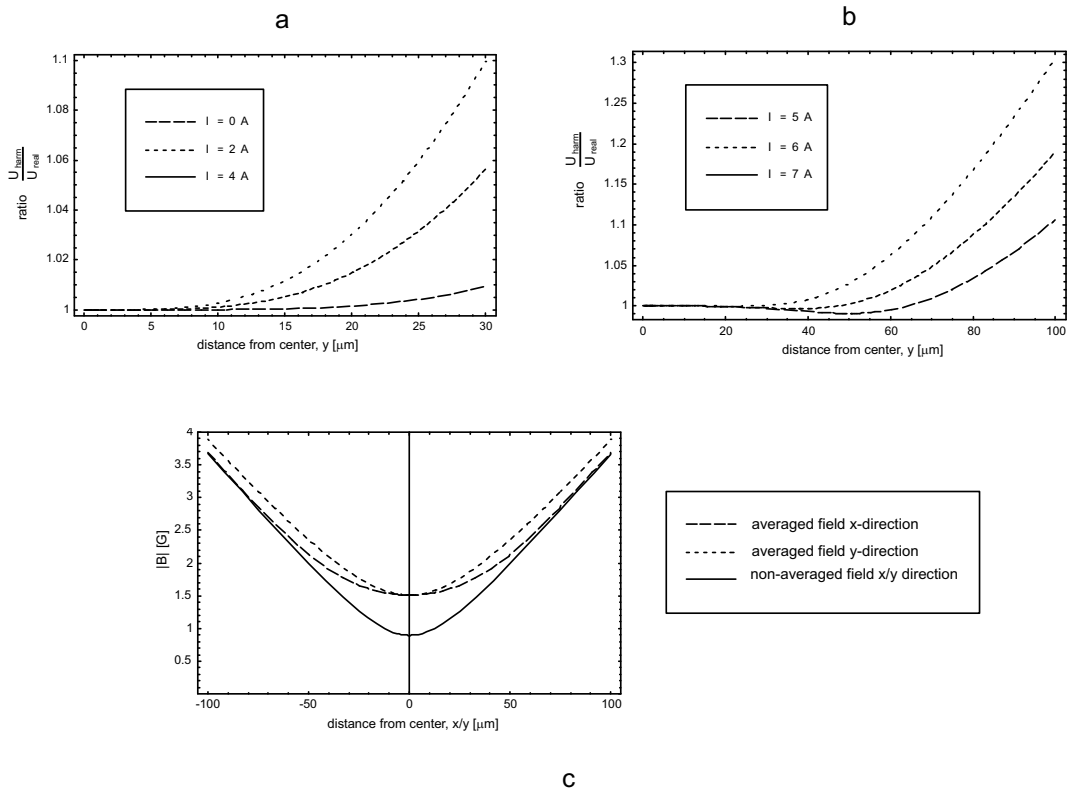
Figure 9.7: *Figure a. and b. show the correction to a harmonic trap in the stretched radial direction as a function of the distance from the center. It is surprising that the harmonic radius increases if the amplitude of the modulation increases. See text for explanation on this. Figure c. shows the trapping potential in x- and y-direction for the averaged and non averaged case.*

Chapter 10

Experimental Results

10.1   Verification of our model

10.1.1   Field produced by Ioffe-helper coil

The model calculated in chapter 8.1.2 is tested by measuring the field produced by one Ioffe helper coil. The results are shown in figure 10.1. The curve plotted is as calculated by the semi-analytical model. A good agreement is found.
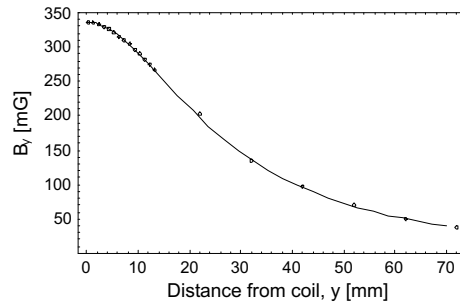
Figure 10.1: *The field as produced by one Ioffe helper coil. The coil carries a current of* $1\,\mathrm{A}$*. The dots indicate the measured values. The line the prediction by the developed model.*

10.1.2   Trap center shift

A static current is applied in Helmholtz configuration to the vertical Ioffe helper coils. This homogeneous field shifts the trap center. The shift is measured to be $6.7\,\mu\mathrm{m/A}$. This differs by 6% from the predicted value ($6.33\,\mu\mathrm{m/A}$). Fitting the model of the main trap to experimental data will give a better agreement. In our system $1\,\mathrm{A}$ corresponds with $0.226\,\mathrm{G}$ in the trap center according to the model.

10.1.3 Offset due to the TOP

From equation (9.5) we see that the TOP increases the offset field. This B_0 is measured as a function of the amplitude of the TOP. The B_0 is measured by scanning the end of the evaporation ramp down. A condensate is obtained before all atoms are lost from the trap. Therefore the last atoms left in the trap have very low energy and we can assume this is the real B_0.

Theoretical calculations were done threefold. First equation (9.5) was used. Second the model was applied to the dressed trap which was then averaged over the TOP cycle (the evaporation is by adiabatic passage, see paragraph 8.3). Third the model was applied by making the assumption that the atoms are non-adiabatically removed from the trap. The latter two resulted in comparable curves of B_0 as a function of the TOP amplitude. The results are shown in figure 10.2.

The measured values experience twice the expected effect of the TOP. This discrepancy remains to be explained.
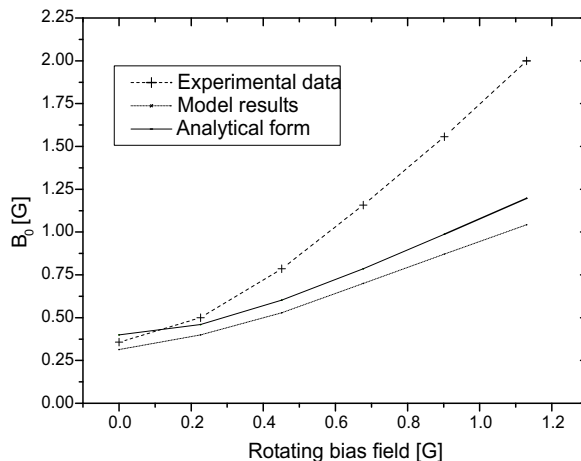
Figure 10.2: *B_0 measurement, see text for explanation of experiment. For our experiment* 1 G *corresponds with* 4.5 A *in the Ioffe helper coils. The crosses are the measured data-points. The first 4 points resulted in a BEC. This indicates that the measured B_0 is the real B_0. The two plots show the B_0 as calculated by our model and as found from formula (9.5) .*

10.2 Double TOP

10.2.1 Displacement

The first derivative of the averaged potential in z-direction is given by:

$$\frac{dU(r,z)}{dz} = \frac{2\beta(B_0 + \beta z^2)}{\sqrt{B_b^2 + (B_0 + \beta z^2)}} z. \tag{10.1}$$

This has a maximum at $z = 0$ and two minima at $z = \pm\sqrt{-B_0/\beta}$ if $B_0 < 0$. From this we see that the displacement of two clouds in the Double TOP is independent of the amplitude of the bias field. During this experiment the amplitude of the TOP was $3\,\text{A}$, corresponding with $0.68\,\text{G}$ in the trap center.

The displacement has been measured as a function of the B_0 in the system. The measurement has been made by cooling a cloud as described in paragraph 9.2.1. The evaporative cooling is performed to an end frequency above the condensation temperature. The B_0 is decreased from $400\,\text{mG}$ down to the measured point in steps of $50\,\text{mG}$ separated in time by $70\,\text{ms}$. The cloud is let to thermalize for $500\,\text{ms}$. An absorption image is taken after $4\,\text{ms}$ expansion time. The center of the clouds is determined by a Gaussian fit through the data points. Figure 10.3 shows the measured points and the curve calculated by the model. The calculated displacement is systematically bigger than the measured displacement. As seen above the displacement is a function of the B_0 and the curvature β in z-direction. If we correct the curvature in our model for the value as measured in the experiment we obtain a better agreement with the measured data points.

The discrepancy seen around zero B_0 is due to the fact that the cloud is stretched at that point. Due to the noise it is hard to distinguish between a stretched cloud with structure and without. Therefore these points should be neglected.
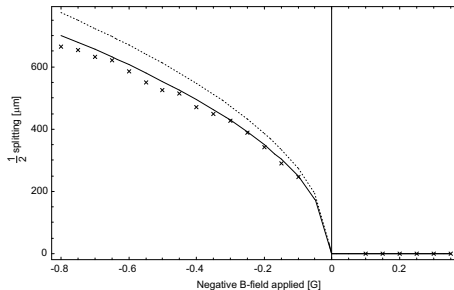
Figure 10.3: *Displacement of a cloud from the trap center due to a negative B0 applied. The dotted curve indicates the results from the model. The line is the result from the model after correction for the measurements done in section 10.1.2. For the points around zero the cloud is stretched and does not have a double component. Therefore it is hard determine the center of the could.*

10.2.2 Axial trapping frequency in double trap

The axial trapping frequency has been measured by oscillating the cloud in axial direction. By determining the center of mass of the cloud as a function of the time one obtains the trapping frequency. The experimental procedure to excite this oscillation is as follows. The B_0 is gently ramped down to a value of $-0.55\,\text{G}$ as explained above. After thermalization of the cloud it is evaporated further to obtain a small dense cloud. Then the B_0 is nonadiabatically jumped to $-0.8\,\text{G}$. This changes the trapping potential instantaneously to one where the cloud is not in its stable state. Therefore the cloud starts to undergo an oscillation in axial direction. The position of the cloud is measured as a function of the holding time in this last potential. The measurement is performed to obtain information on the trapping frequency. Therefore the timespan of the measurement is too short to obtain any information on damping of the oscillation. The data points have been fitted to a sine (see figure 10.4). The trapping frequency derived from this fit is: $\omega_z = 2\pi \cdot 26.8(1)\,\text{Hz}$. Our model gives $2\pi \cdot 28.7\,\text{Hz}$. If we force agreement with radial displacement measurements as seen in paragraph 10.1.2 we obtain from our model: $2\pi \cdot 27.9\,\text{Hz}$, differing by 4% from the measured value. The amplitude of this oscillation is of the order of $100\,\mu\text{m}$. In this region axial anharmonicities become important. This effect lowers the real trapping frequency for high amplitude oscillations as compared to low amplitude oscillations.
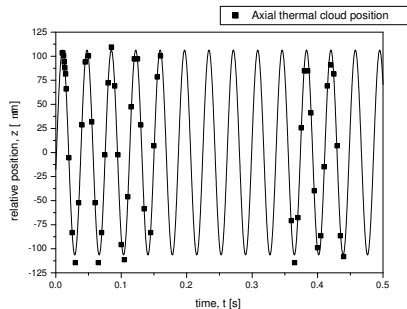
Figure 10.4: *Center of mass oscillation of a could in one well of the double trap. The line indicates a fit to a non-decaying sine wave. The fit corresponds to a frequency of $\omega_z = 2\pi \cdot 26.8(1)\,\text{Hz}$*

10.2.3 Anharmonic trap

For small positive B_0 values the trap becomes anharmonic in z-direction. This can be explained from formula (9.5) . The averaged B_0 increases more for the points where the non-averaged B_0 is close to zero. This effect 'flattens' the lowest part of the well. Trapping a cloud in such a well results in a cloud stretched in

axial direction. To prove this effect a measurement has been made by switching the trap from a stable harmonic trap instantaneously to this anharmonic region. The trapped thermal cloud has the density profile corresponding to a harmonic trap. The flattening of the trap bottom reduces the axial confinement around the trap center. The cloud undergoes an oscillation by splitting up in two more dense parts, and coming back in the center after this oscillation. The images in figure 10.5 show the density distribution as a function of the holding time in the anharmonic trap. This proves the possibility to tune the anharmonicities in axial direction. No quantitative measurements have been performed on this aspect.

10.3 Double BEC

Cooling to two Bose Einstein Condensates in the Double TOP has been realized. To proof a cold cloud is really a condensate generally two methods are used. To be able to understand these two criteria extra theory on Bose Einstein Condensation has to be done.

10.3.1 Theory of determination of a BEC

Cold gases of temperatures below the critical temperature $(T < T_c)$ can be described by the so-called Gross-Pitaevskii equation [29]

$$\left(-\frac{\hbar^2\nabla^2}{2m} + U(\mathbf{r}) + g|\phi(\mathbf{r})|^2\right)\phi(\mathbf{r}) = \mu\phi(\mathbf{r}), \qquad (10.2)$$

where $\phi(\mathbf{r})$ is the macroscopic wavefunction describing the condensate, $U(\mathbf{r})$ the trapping potential and g is the interaction parameter given by: $g = 4\pi\hbar^2 a/m$, with a the scattering length. At high densities and positive a the mean-field interaction, given by the third term on the left, becomes dominant over the kinetic energy term, given by the first term from the left. Therefore the kinetic energy term can be neglected. This is called the Thomas-Fermi approximation. [29] In this approximation equation (10.2) can be solved easily. The density distribution in the condensate is now given by:

$$n_{BEC}(\mathbf{r}) = |\phi(\mathbf{r})|^2 = \frac{1}{g}(\mu - U(\mathbf{r})) \qquad (10.3)$$

We see that the density profile is inversely proportional to the trapping potential. Therefore in the case of a harmonic potential the density profile becomes parabolic:

$$n_{BEC}(\mathbf{r}) = n_{BEC}(0)\left(1 - \left(\frac{x}{x_0}\right)^2 - \left(\frac{y}{y_0}\right)^2 - \left(\frac{z}{z_0}\right)^2\right) \qquad (10.4)$$

It can be shown that for a hot thermal cloud in a harmonic trap the density distribution is given by a Gaussian distribution [18]:

$$n_{th}(\mathbf{r}) = n_{th}(0) \prod_i e^{-(r_i/L_i)^2}, \tag{10.5}$$

with $i \in \{x, y, z\}$ where $L_i = \sqrt{2k_b T/m\omega_i^2}$, with ω_i the trapping frequency in direction i.

As explained in the general introduction measurements in BEC experiments generally consist of an absorption image. Essentially this is an integration of the density along one coordinate. From the Lambert-Beer law (3.16) it shows that the detected optical density is proportional to the column density. For the thermal distribution the column density is given by:

$$
\begin{aligned}
CD_{th} &= \int_{x=-\infty}^{\infty} n_{th}(0) e^{-\left(\frac{x}{x_0}\right)^2 + \left(\frac{y}{y_0}\right)^2 + \left(\frac{z}{z_0}\right)^2} dx \tag{10.6} \\
&= x_0 \sqrt{\pi} n_{th}(0) e^{-\left(\left(\frac{y}{y_0}\right)^2 + \left(\frac{z}{z_0}\right)^2\right)} \tag{10.7}
\end{aligned}
$$

where x is the direction of propagation of the light. We see that the column density is described by a Gaussian. For a condensate in a harmonic trap we obtain:

$$
\begin{aligned}
CD_{BEC} &= \int_{x=-X_{int}}^{+X_{int}} n_{BEC}(0) \left(1 - \left(\frac{x}{x_0}\right)^2 - \left(\frac{y}{y_0}\right)^2 - \left(\frac{z}{z_0}\right)^2\right) dx \\
&= n_{BEC}(0) \left[x\left(1 - y^2 - z^2\right) - \frac{1}{3}x^3 \right]_{x=-X_{int}}^{x=+X_{int}} \\
&= \frac{4}{3} n_{BEC}(0) \left(1 - y^2 - z^2\right)^{\frac{3}{2}} \tag{10.8} \\
X_{int} &= \sqrt{1 - \left(\frac{y}{y_0}\right)^2 - \left(\frac{z}{z_0}\right)^2}
\end{aligned}
$$

The integration limits $\pm X_{int}$ have to be chosen such that the density distribution does not become negative. From this result we see that the absorption images have to be fitted to equation (10.8).

We can distinguish now the difference between a hot thermal cloud and a condensate by looking at the density distribution of the atoms. If this results in a Gaussian shape the cloud is non-condensed, if it results in equation (10.8) the cloud it is condensed. By fitting the density to a Gaussian distribution with an inverted parabola on top of it one can also determine the fraction of condensed atoms in the sample.

Expansion If the Thomas-Fermi approximation is assumed, the cloud has a parabolic shape as seen above. If the trapping potential is switched off completely the cloud expands freely. It can be shown that during this expansion

the parabolic distribution of the cloud is preserved [34]. In the limit of a large aspect ratio of the unexpanded cloud ($\beta = \omega_z/\omega_\rho \ll 1$) and $\omega_\rho\tau \gg 1$ the radii of the condensate are given after an expansion time τ by [35]:

$$
\begin{aligned}
R_\rho(t_{exp}) &= R_\rho(0)\sqrt{1 + \omega_\rho^2\tau^2} & (10.9)\\
R_z(t_{exp}) &= R_z(0)\left[1 + \beta\omega_z\tau\arctan(\omega_\rho\tau)\right] & (10.10)
\end{aligned}
$$

It is clear that the radial size (given by equation (10.9)) expands much faster than the axial size (given by equation (10.10)). If we now look after a certain expansion time the cloud has become spherical. After even longer expansion the radial size is bigger than the axial size and the expanded cloud becomes a pancake.

For a thermal cloud the kinetic energy term dominates over the mean-field interaction term. The kinetic energy is an isotropic property of the sample. Therefore the expansion of a thermal cloud is isotropic and leads for long times to a spherical cloud.

Concluding, by looking at the expansion of a sample one can determine the fact if there is a condensate or not. In the case of a mixed sample the thermal part will blow away spherically and in the center a dense part will be expanding mainly in radial direction.

10.3.2 Experimental proof of BEC

As explained above by looking at the density distribution one can distinguish between a thermal cloud and a BEC. Figure 10.6b shows an absorption image of two clouds above T_c after $4\,\mathrm{ms}$ of expansion time. The clouds have been cooled as described above. The evaporation end-frequency was $\nu_{RF,end} = 900\,\mathrm{kHz}$. The B_0 has been measured to be $\nu_0 = 767(2)\,\mathrm{kHz}$ in this series of measurements. In figure 10.6a an axial cut through the center of the left cloud is shown. The line shown is a Gaussian fit to the optical density. It is clear that this cloud is not condensed.

The same measurement is repeated, but now with an evaporation end frequency of $\nu_{RF,end} = 790\,\mathrm{kHz}$, corresponding to $23\,\mathrm{kHz}$ above B_0. Again an absorption image and an axial cut through the left cloud is shown in figure 10.7a and 10.7b. The line is a fit to formula (10.8) . It is clear that this cloud is a pure condensate. To our knowledge two Bose Einstein Condensates created in a Ioffe quadrupole trap by purely magnetic means has never been reported before. By making use of a light sheet repulsive to the atoms Andrews, et. al. [36] obtained two condensates in an Ioffe quadrupole trap. However, these condensates are highly asymmetrical.

10.3.3 Lifetime in the split trap

The lifetime of a thermal cloud in the double trap has been measured. The experimental procedure was as follows. The cloud was split as explained above. The intermediate evaporation frequency $\nu_{RF,int}$ (see section 9.2.1) was set to a value of 1.8 MHz to obtain a dilute cloud. The end evaporation frequency $\nu_{RF,end}$ was set to a value of 900 kHz to obtain a non-condensed cloud. The number of atoms has been measured as a function of the plain evaporation time τ_{plain}.

Lifetime with TOP Two series of measurements have been made. One series with the TOP on during the plain evaporation and one series with the TOP switched off at the start of the plain evaporation. Figure 10.8 shows the results with the TOP on. Atoms can reach the energy of the plain evaporation frequency due to collisions. This process will remove atoms from the trap. Collisional processes occur with a certain probability. As one can see from figure 10.8 the decay process cannot be fit to a single exponential decay. Reasons for this can be the fact that the position of the cloud in the trap is not stable. The center position of the cloud varied within 8 μm over this series of measurements. This can be due to a center of mass oscillation of the cloud. The cloud is calculated to have a $1/e$-radius of 4.5 μm in the trap. With fluctuations of at maximum 8 μm the cloud cannot reach the circle of death (20 μm). Therefore this does not generate detectable extra losses.

The explanations of which processes *can* induce losses are rather speculative. One explanation is that the wings of the cloud are moved through the RF-evaporation radius due to this oscillation. This performs extra evaporative cooling, and generates extra losses. However, after a certain time the cloud has become smaller due to the losses. At that time the evaporation point is not reached anymore and the decay process slows down. This would explain the two exponential fits shown in figure 10.8. However, the evaporation process in our time-dependant trap is not fully understood. Therefore no calculations could be made to verify this statement.

Lifetime without TOP The measurement as described above has been repeated without the TOP. The experimental scheme was almost the same as above. The only change was that the TOP has been turned off at the starting point of the plain evaporation. Again the number of atoms has been measured as a function of the plain evaporation time. Figure 10.9 shows the results. A decrease in atom number has been observed until 14 ms after the TOP has been switched off. From that point on no atoms were left in the trap. This is attributed to Majorana loss. The decay process depends on the size of the region where the magnetic field is smaller than the Larmor frequency. In this region the field changes direction. The atoms are actively depolarized. We therefore do not expect an exponential decay. However, the axial trapping frequency has

73

been measured to be $\omega_z = 2\pi \cdot 26.8\,\text{Hz}$ as presented in paragraph 10.2.2. This corresponds to an oscillation period of: $37\,\text{ms}$. All atoms have passed the point of zero-magnetic field after half an oscillation period. If the losses are very efficient, all atoms would be lost after $18\,\text{ms}$. This trapping frequency is derived for an harmonic trap. In the case without the TOP the trap is not harmonic over the region of the cloud. Therefore the atoms are moved slightly faster towards the center. This implies a lifetime off less than $18\,\text{ms}$. This might explain the lifetime of the cloud being $14\,\text{ms}$ as we observed.

10.4   Colliding condensates

No quantitative measurements have been made on the collisional properties of Bose Einstein Condensates. However, it has been qualitatively demonstrated to show the possibilities of having two condensates in a Ioffe quadrupole trap.

The two condensates trapped in the Double TOP have been accelerated towards each other. This is done by instantaneously switching the trapping potential from the double TOP back to the original harmonic trap. The confinement of the condensates is not affected by this. Therefore no shape-oscillations are induced. The axial position of the condensates in the harmonic trap at time t is simply given by:

$$z_c(t) = \pm A \cdot \cos(\omega_z t) \tag{10.11}$$

where at time $t = 0$ the potential is switched to the harmonic potential. The distance between the two condensates is $2\,A$ at time $t = 0$. The relative velocity of the two condensates at the colissional point ($z = 0$) is given by:

$$v_{rel} = 2|\dot{z}_c(t_c)| = 2\omega_z A \tag{10.12}$$

where t_c is the time of the collision occurring, given by $t_c = \pi/(2\omega_z)$. The atoms in the condensates do not collide if the relative velocity *of the condensates* is smaller than the critical velocity in the condensate. However, if the velocity is higher than the critical velocity atoms get scattered out of the condensate. This scattering has first been measured by Raman, et al. [37]. The collisional process in a condensate has been observed by Stenger, et al. [38]. The experiment was done by means of Bragg spectroscopy. Two beams were counter propagated through an elongated BEC. The condensate absorbs momentum from both beams. This simulates a collision. It was observed that below the speed of sound little momentum was transferred to the condensate.

The speed of sound is given by:

$$c = \sqrt{\frac{g\,n}{m}}, \tag{10.13}$$

$$g = \frac{4\pi\hbar^2 a}{m} \tag{10.14}$$

with g, the coupling constant to the potential, n the density and a the scattering length. For our case the speed of sound is calculated to be: $c = 6.15\,\text{mm/s}$.

We collided two condensates at a speed large ($v_{rel} = 27.4[mm/s]$) compared to the speed of sound. A movie of this collision is shown in figure 10.10. After the collision we observe a shockwave of atoms flying out from the collisional point. These scattered atoms undergo an oscillation in the trap. The radial trapping frequency is of the order of $400\,\text{Hz}$ therefore the time for half an oscillation is: $\frac{1}{2\cdot400} = 1.25\,\text{ms}$. This corresponds to the time interval that the atoms disappear and reappear on z-axis as is observed for expansion times: $15-18\,\text{ms}$). The stripe indicates the concentration of the atoms on the axis.
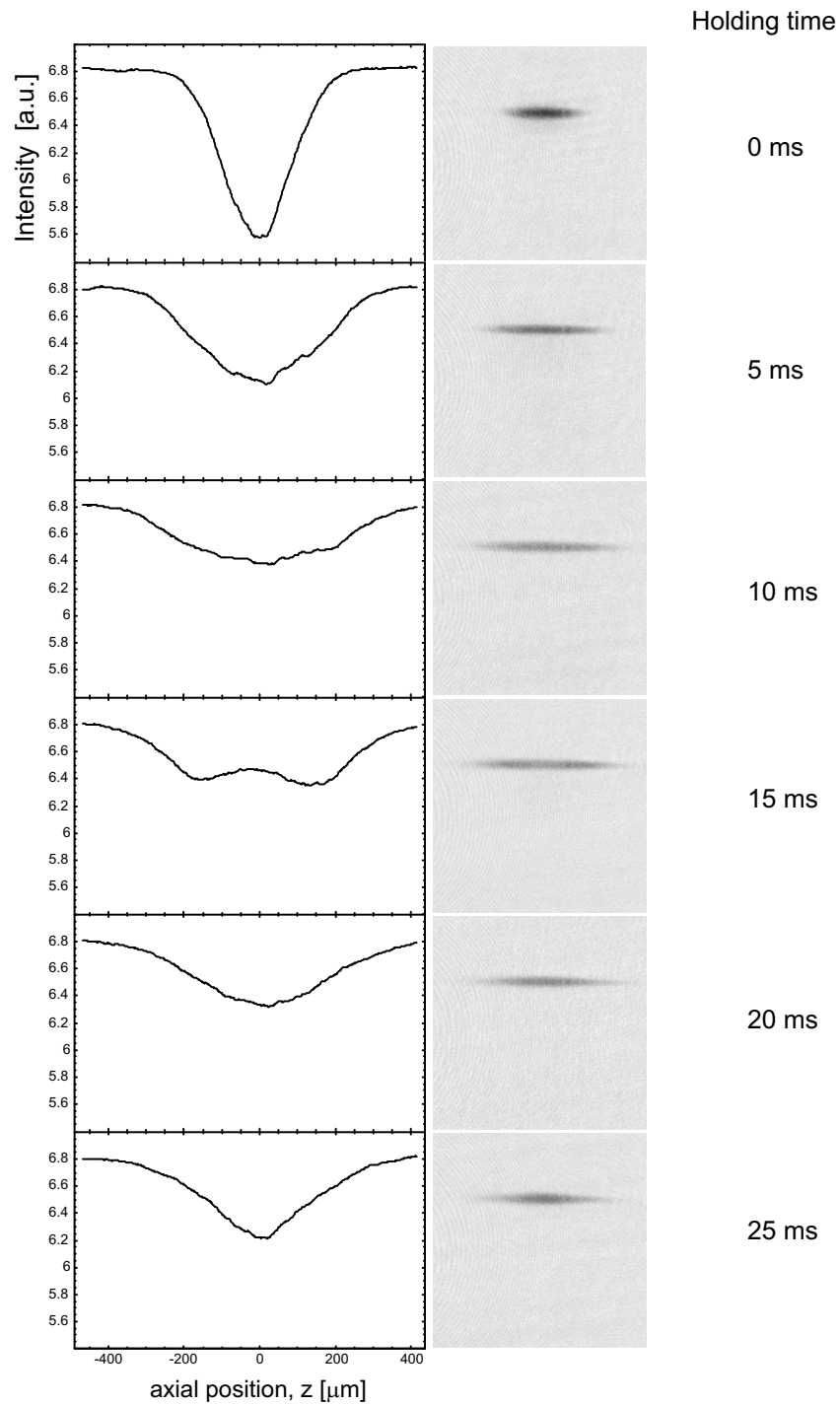
Figure 10.5: *Anharmonic trap oscillation. The trap is switched from a harmonic trap instantaneously to a anharmonic trap with a flattened bottom. It is clear that two parts move outside and back inside again. This measurement is taken with a thermal cloud.*
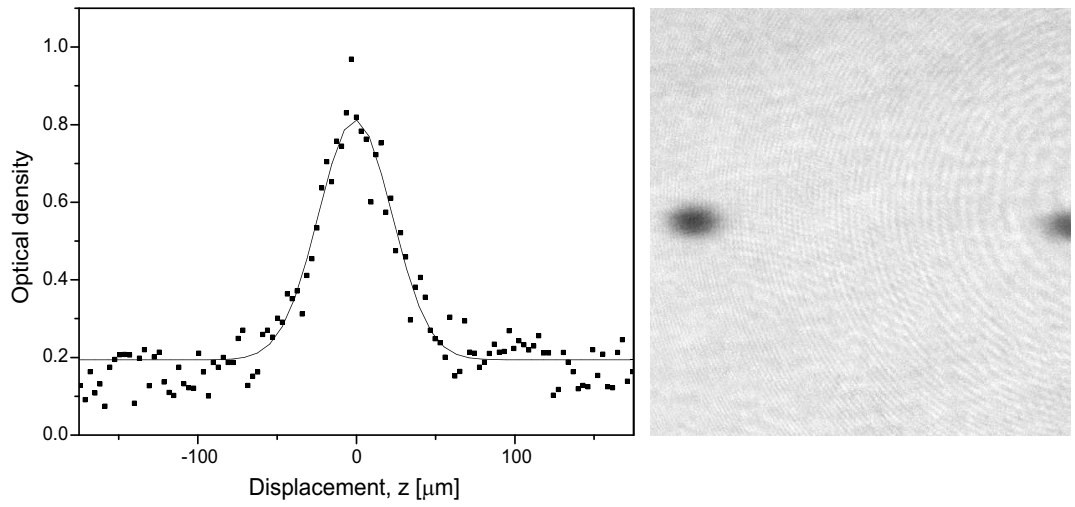
Figure 10.6: *An absorption image of a double cloud after* 4 ms *of expansion time.* $\nu_{RF,end} = \nu_0 + 133$ kHz. *Both clouds are visible. The left image shows an axial cut through the left cloud. The fit corresponds to formula (10.7) . It is clear that this cloud is not condensed.*
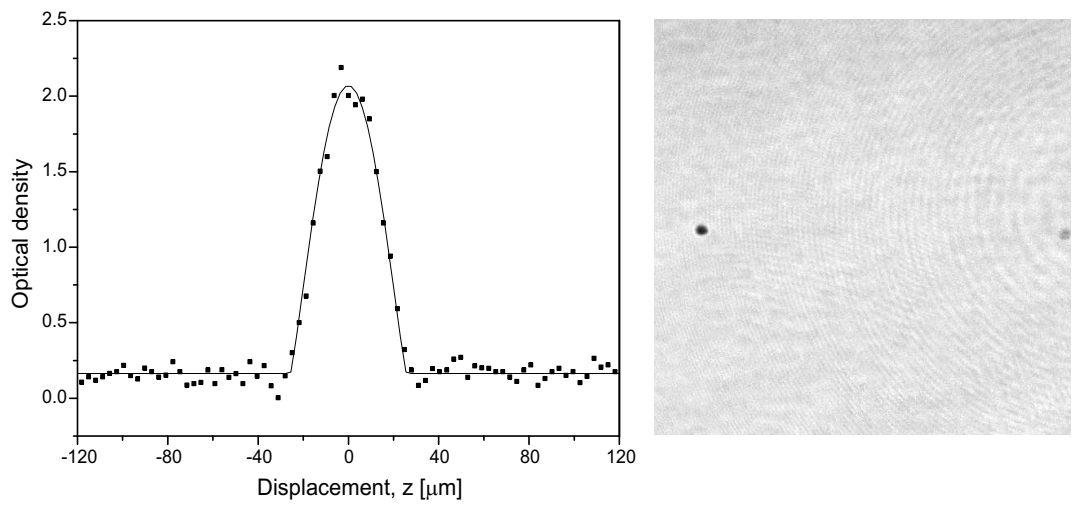
Figure 10.7: *An absorption image of a double cloud after* 4 ms *of expansion time.* $\nu_{RF,end} = \nu_0 + 23$ kHz. *The right cloud is very faint. This is because the camera is under an angle and is focused on the left cloud. The left image shows an axial cut through the left cloud. The fit corresponds to formula (10.8) . It is clear that this cloud is a BEC.*
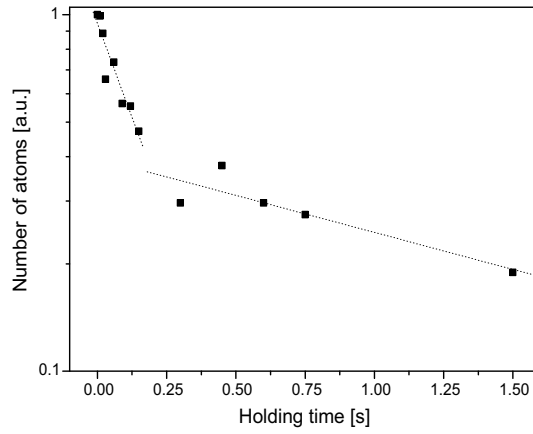
Figure 10.8: *The lifetime of a thermal cloud in the double TOP. The fits are to two exponential decays. This is a speculative explanation for the data. See text for more details.*
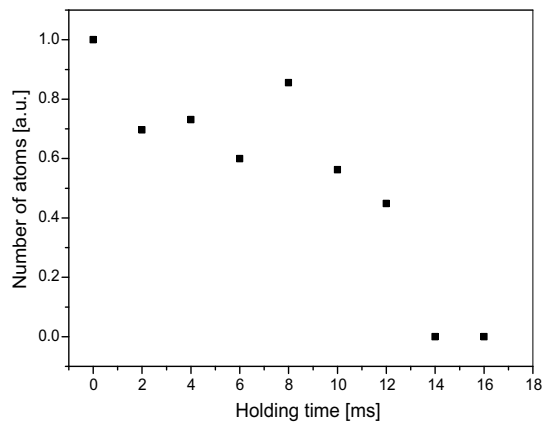
Figure 10.9: *The lifetime of a thermal cloud in the double trap. After the normal splitting method the TOP is turned off. After 14 ms no atoms are left. See text for more details.*
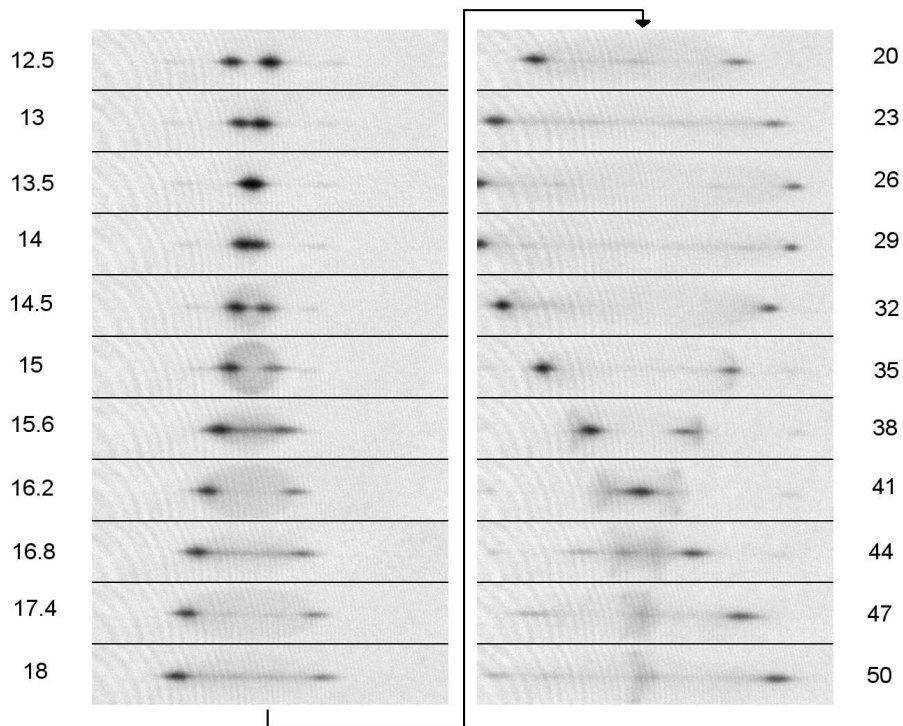
Figure 10.10: *A movie of the collision of two Bose Einstein Condensates.* $\nu_{RF,end} = \nu_0 + 50\,\text{kHz}$. *One should note that the series on the left has time-intervals of* $0.6\,\text{ms}$ *and the series on the right* $3\,\text{ms}$. *After the collision (holding time of* $12\,\text{ms}$*) a shockwave of scattered atoms is observed. These scattered atoms undergo an oscillation in the trap.*

Chapter 11

Conclusion

A very complete model describing the trapping potential has been developed. Although the approach is crude and does not result in an analytical form it has proven to be very powerful. As a result of this model various new type of experiments in Ioffe-Quadrupole traps have been presented. The first realization of two Bose Einstein Condensates in a Ioffe-Quadrupole trap by purely magnetic means has been demonstrated. The collisional process has been demonstrated briefly by colliding two condensates.

Appendices

Appendix A

Bessel Functions

A.1 Frequency modulation

Suppose a field is oscillating at angular frequency ω. The frequency is modulated with frequency ω_M and amplitude A in frequency space. The field is then given by:

$$E(t) = E_0 \sin\left(\omega t + A \sin \omega_M t\right). \tag{A.1}$$

To solve this equation we make use of Jacobi's expansions of the two functions [15]:

$$
\begin{aligned}
\cos(z \sin \theta) &= J_0(z) + 2 \sum_{n=1}^{\infty} J_{2n}(z) \cos 2n\theta \\
\sin(z \sin \theta) &= 2 \sum_{n=0}^{\infty} J_{2n+1}(z) \sin(2n+1)\theta
\end{aligned}
\tag{A.2}
$$

where $J_n(a)$ is the Bessel coefficient of order n and argument a. A general property of Bessel function is that $J_{-n}(z) = (-1)^n J_n(z)$. Therefore we can write (A.2) as:

$$
\begin{aligned}
\cos(z \sin \theta) &= \sum_{n=-\infty}^{\infty} J_{2n}(z) \cos 2n\theta \\
\sin(z \sin \theta) &= \sum_{n=-\infty}^{\infty} J_{2n+1}(z) \sin(2n+1)\theta
\end{aligned}
$$

We can also state:

$$
\cos(z \sin \theta) = \sum_{n=-\infty}^{\infty} J_{2n}(z) \cos 2n\theta
$$

82

$$\sin(z\sin\theta) \quad = \quad \sum_{n=-\infty}^{\infty} J_{2n+1}(z)\sin(2n+1)\theta \qquad (A.3)$$

because the terms with positive order cancel with the corresponding terms with negative order. Therefore we can rewrite equations A.3 as:

$$\cos(z\sin\theta) \quad = \quad \sum_{n=-\infty}^{\infty} J_n(z)\cos n\theta$$

$$\sin(z\sin\theta) \quad = \quad \sum_{n=-\infty}^{\infty} J_n(z)\sin n\theta \qquad (A.4)$$

If we now make use of:

$$\sin(a+b) = \sin a\cos b + \cos a\sin b \qquad (A.5)$$

we can combine (A.1) and (A.4) to obtain:

$$
\begin{aligned}
E(t) \quad &= \quad E_0\sin\left(\omega t + A\sin\omega_M t\right)\\
&= \quad E_0\left[\sin\omega t\cos(A\sin\omega_M t) + \cos\omega t\sin(A\sin\omega_M t)\right]\\
&= \quad E_0\left[\sin\omega t\sum_{n=-\infty}^{\infty} J_n(A)\cos n\omega_M t\right.\\
&\qquad\qquad \left. + \cos\omega t\sum_{n=-\infty}^{\infty} J_n(A)\sin n\omega_M t\right]\\
&= \quad E_0\sum_{n=-\infty}^{\infty} J_n(A)\left(\sin\omega t\cos n\omega_M t + \cos\omega t\sin n\omega_M t\right)\\
&= \quad E_0\sum_{n=-\infty}^{\infty} J_n(A)\sin(\omega t + n\omega_M t) \qquad (A.6)
\end{aligned}
$$

A.2   Amplitude modulation

An oscillating field can generally be described by:

$$E(t) = E_0\cos(\omega t + \phi_0) \qquad (A.7)$$

We choose the offset phase zero ($\phi_0 = 0$). In amplitude modulation processes E_0 is varied. If we apply an sinusoidal amplitude modulation to equation (A.7) we obtain:

$$E(t) = E_0(1 + A\cos\omega_M t)\cos\omega t \qquad (A.8)$$

where ω_M is the modulation frequency and A is the modulation depth. By means of simple trigonometry we can rewrite equation (A.8) as:

$$E(t) = E_0 \left[\cos \omega t + \frac{A}{2} \cos(\omega + \omega_M)t + \frac{A}{2} \cos(\omega - \omega_M)t \right] \qquad \text{(A.9)}$$

Here we see two sidebands appear which are in phase. This distinguished amplitude modulated signals from frequency modulated ones.

Appendix B

Laser setup

B.1   Slave mount

The design goal of the source laser system was frequency stability. This required the development of a new slave laser mount. Previously used housings were lacking stability for our purposes. The previously used mount was manufactured by Newport (model *700C*). A schematic drawing is shown in figure B.1. Unstable aspects of this design are for example that the laser diode is mounted on the Peltier element. The other side of the Peltier element is mounted on the housing. This housing holds the collimator lens. Changes in the temperature difference between the diode and the mount changes the relative position of the diode and the lens. This makes the collimation of the beam less stable.

A rather unstable effect is the mounting of the collimator lens. The lens is mounted in a threaded hole. The lens is adjusted to the right position by screwing it in and out. The position of the lens is not stable because the tread has backlash.

A new mount has been developed to obtain a more stable solution. Figure B.2 shows a drawing of the mount. The mount is designed to have a low thermal mass. Therefore the bandwidth of the feedback of the temperature stabilization is larger. The laser diode and collimator lens are connected to each other without any moveable parts. A translation stage is used to optimize the position of the collimator lens. Two rods of the appropriate diameter are dropped into the empty space. These are glued to the mount and to the lens. The mount is expected to be more stable. No deviations could be detected at the time of writing this report.
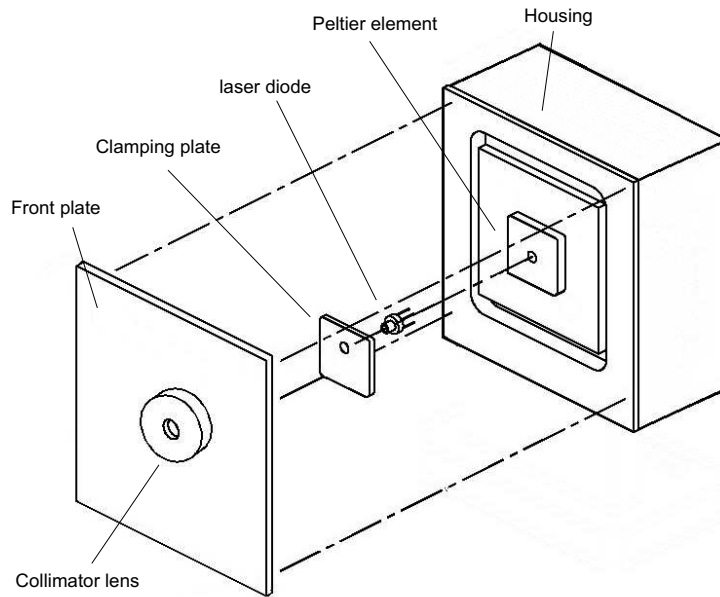
Figure B.1: *Schematic drawing of the previously used Newport mount. The diode is directly mounted on the peltier element. Temperature fluctuations changes the alignment of the diode.*
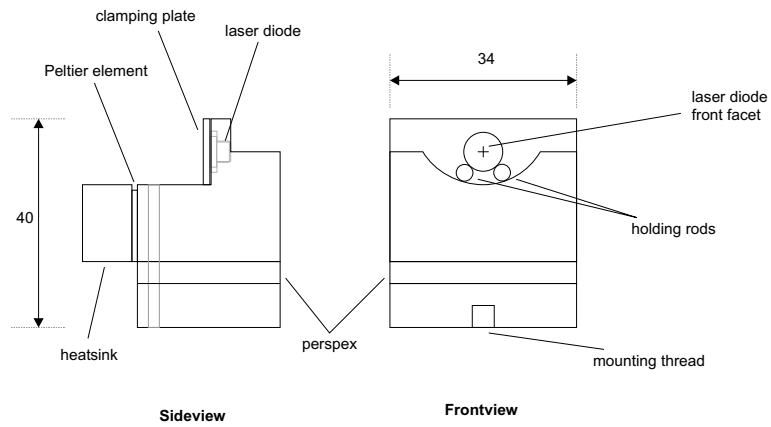
Figure B.2: *Slave laser mount, measures are in mm. The mount is made of aluminium except for the layer of perspex. The aluminium is to have a good thermal contact between the diode and the peltier. The perspex is to make the diode electrically disconnected from the ground.*

Figure B.3: *photograph of the lasermount. The euro-cent coils are to indicate the scale.*

Appendix C

Ioffe helper coil derivations

Curvature   Figure C.1 shows a Ioffe-helper coil. The denoted dimensions are listed in table C. The magnetic field produced by an wire segment carrying a current I is given by the Biot-Savart law 8.6

$$\mathbf{B}(\mathbf{r}) = \frac{\mu_0}{4\pi} I \int \frac{d\mathbf{l}' \times \mathbf{r}}{r^3}, \tag{C.1}$$

where the integral is evaluated over the wire. The wire length element $d\mathbf{l}'$ pointing along the direction of the current and the vector $\mathbf{r}'$ are given by:

$$d\mathbf{l}' = dl \begin{pmatrix} -\sin\theta \\ 0 \\ \cos\theta \end{pmatrix} = a\, d\theta \begin{pmatrix} \sin\theta \\ 0 \\ \cos\theta \end{pmatrix} \tag{C.2}$$

$$\mathbf{r}' = \begin{pmatrix} a\cos\theta \\ y_0 \\ h + a\sin\theta \end{pmatrix} \tag{C.3}$$

The magnetic field at point $\mathbf{r} = (x, y, z)$ produced by the upper curvature is given by:

$$\mathbf{B}_{curv}(x, y, z) = \frac{\mu_0}{4\pi} I \int_{curv} d\theta \frac{1}{|\mathbf{r}' - \mathbf{r}|^3} d\mathbf{r}' \times (\mathbf{r}' - \mathbf{r}) \tag{C.4}$$

$$= \frac{\mu_0}{4\pi} I \int_{curv} d\theta \frac{1}{|\mathbf{r}' - \mathbf{r}|^3} \begin{pmatrix} -\sin\theta \\ 0 \\ \cos\theta \end{pmatrix} \times \begin{pmatrix} a\cos\theta - x \\ y_0 - y \\ h + a\sin\theta - z \end{pmatrix} \tag{C.5}$$

Simplifying the outer product results in the following integral for the upper curvature:

$$\mathbf{B}_{curv}(x, y, z) = \frac{1}{a_{out} - a_{in}} \int_{\theta=0}^{\pi} \int_{r=a_{in}}^{a_{out}} \begin{pmatrix} -(y_0 - y)\cos\theta \\ r - x\cos\theta + h\sin\theta - z\sin\theta \\ -(y_0 - y)\sin\theta \end{pmatrix}$$

measure	symbol	value
inner radius	a_{in}	18 mm
outer radius	a_{out}	36 mm
rod length	$2H$	79 mm
displacement from coordinate origin	y_0	-37 mm

Table C.1: The magnitudes of the measures as used in the numerical calculation.

$$\cdot \frac{1}{\left((y_0 - y)^2 + (a\cos\theta - x)^2 + (h - z + a\sin\theta)^2\right)^{3/2}} \quad \text{(C.6)}$$

The integration limits are denoted in figure C.1.
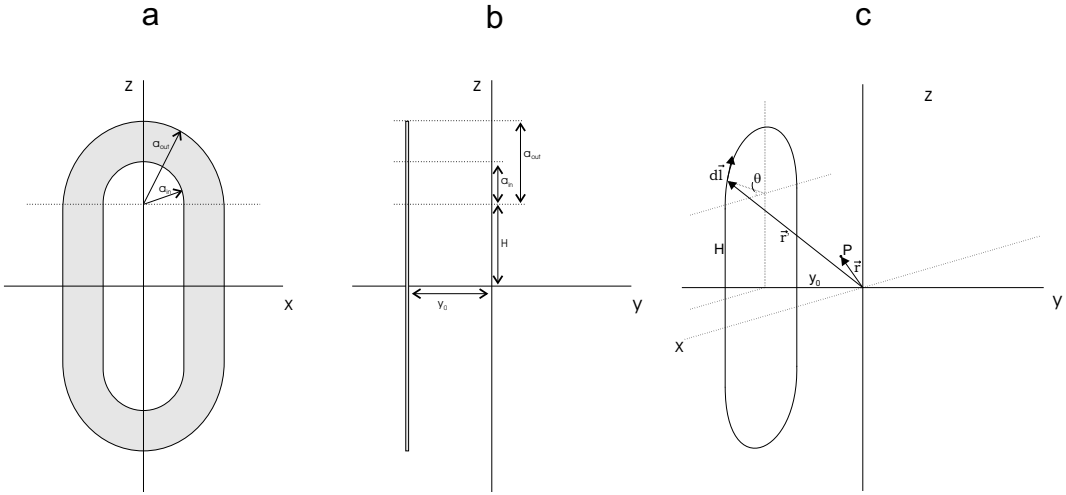
Figure C.1: *Ioffe-helper coil shown in three perspectives. Figure a. and b. show the view along the y and x-axis respectively. Figure c. shows a three-dimensional figure of the coil. The coil is drawn as a the infinitely thin wire which is integrated over the region of the copper.*

Rod For one of the straight parts the vectors in the integral $d\mathbf{l}$ and r' are written as:

$$d\mathbf{l} = \begin{pmatrix} 0 \\ 0 \\ dl \end{pmatrix} = |\mathbf{r} - \mathbf{r}'| \begin{pmatrix} 0 \\ 0 \\ 1 \end{pmatrix} d\theta \quad \text{(C.7)}$$

$$\mathbf{r}' = \begin{pmatrix} a - x \\ y_0 - y \\ z' - z \end{pmatrix} \quad \text{(C.8)}$$

89

Including this in 8.6 we can write the magnetic field as:

$$
\begin{aligned}
\mathbf{B}_{rod}(x, y, z) &= \frac{\mu_0}{4\pi} I \int_{z'=-H}^{+H} d\theta \frac{1}{|\mathbf{r}' - \mathbf{r}|^2} d\mathbf{l} \times \mathbf{r}' \\
&= \frac{\mu_0}{4\pi} I \int_{z'=-H}^{+H} d\theta \begin{pmatrix} -(y_0 - y) \\ a - x \\ 0 \end{pmatrix} \\
&\quad \cdot \frac{1}{((y_0 - y)^2 + (a\cos\theta - x)^2 + (h - z + a\sin\theta)^2)^{3/2}} \quad \text{(C.9)}
\end{aligned}
$$

Equations C.6 and C.9 are to be evaluated numerically.

Appendix D

Rubidium properties
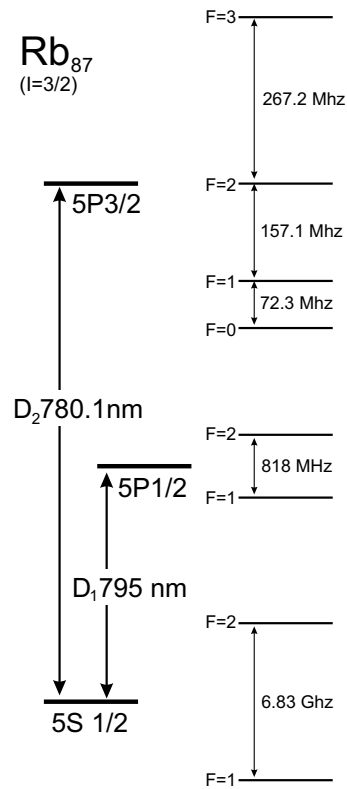
Figure D.1: *The energy level scheme of the two lowest excited* [87]Rb*levels. The spacing of the levels are indicated in Mhz and nm.*
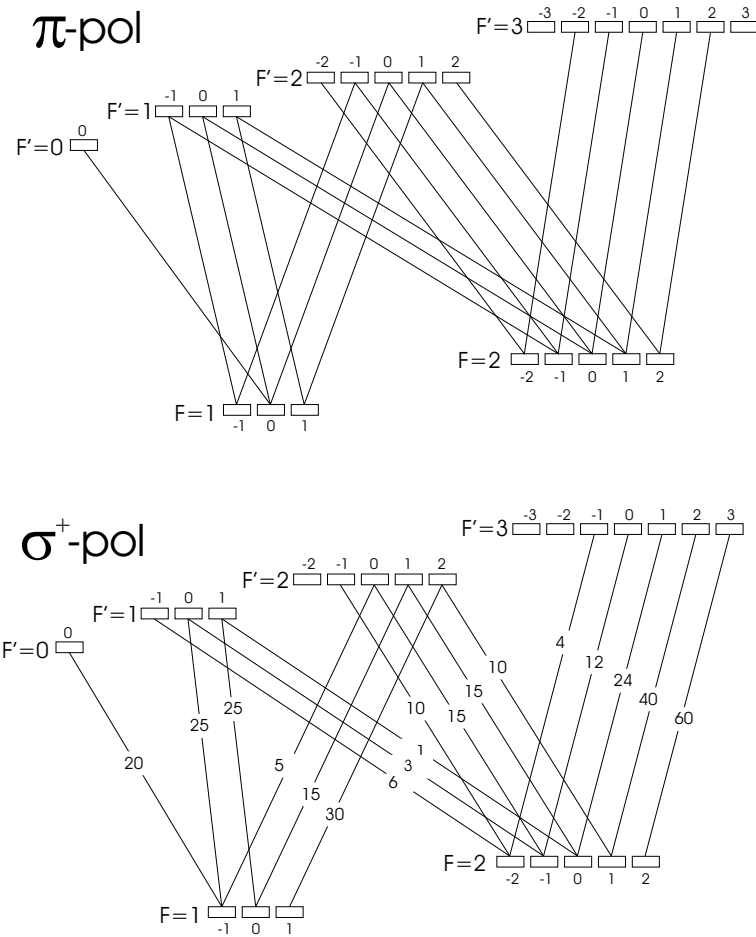
Figure D.2: *The transition probabilities as derived from the Clebsch-Gordan coefficients for $^{87}\text{Rb}D_2$ line. The numbers next to the rectangles indicate the Zeeman sublevel characterized by m_F. The transition probabilities are normalized such that the probabilities are integers. For the σ^- polarization one can change all the m_F numbers to $-m_F$ in the σ^+ diagram.*

Bibliography

[1] S. N. Bose, Z. Phys., **26** (178), 1924

[2] A. Einstein, Sitzber. Kgl. Preuss. Akad. Wiss., **3**, 1925

[3] M. H. Anderson, et. al, *Observation of Bose Einstein Condensation in a dilute atomic vapour* Science, **269** (198), 1995

[4] M. D. Barrett, et. al, *Frequency Stabilization of a Co2 Laser at 3 X 10(-15) and Search for a Parity Violation Effect in Chiral Molecules* Annales De Physique **23** (225), 1998

[5] A. L. Schawlow and C. H. Townes, *Infrared and Optical Masers*, Physical Review **6** (1940-1949), 1958

[6] T. H. Maiman, *Stimulated Optical Radiation in Ruby*, Nature **187** (493) 1960

[7] C. Daussy, et. al, *Semiconductor Lasers*, (Howard W. Sams, Indianapolis 1972)

[8] R. W. Campbell and F.M. Mims, *Semiconductor Lasers*, (Howard W. Sams, Indianapolis 1972)

[9] W. Demtröder, *Laser Spectroscopy, Basic Concepts and Intrumentation*, 2nd printing (Springer-Verlag 1982)

[10] C. Kittel and H. Kroemer, *Thermal Physics*, Second edition, (W. H. Freeman, New York 1997)

[11] W. R. Bannet, *Hole-burning effects in a He-Ne optical maser*, Phys. Rev. **126**, (580) 1962

[12] W. E. Lamb, *Theory of an optical maser*, Phys. Rev. **134A**, (1429), 1964

[13] H. J. Metcalf, P. v/d Straten, *Laser Cooling and Trapping*, (Springer-Verlag 1999)

[14] S. Nakayama, *Theoretical Analysis of Rb and Cs D_2 Lines in Doppler-Free Spectroscopic techniques with Optical Pumping*, Japanese Journal of Applied Physics, **24** (1) 1984

[15] G. N. Watson, *Theory of Bessel Functions*, Second edition (Cambridge, University Press 1962)

[16] H.S. Lee, et. al, *Zeeman effect in the saturation spectroscopy of the 87Rb D2 line*, J. Opt. Soc. Am. B **11** (558), 1994

[17] C. Wieman and T. W. Hänsch *Doppler-Free Laser Polarization Spectroscopy*, Phys. Rev. Lett. **36** (1170), 1976

[18] K. Dieckmann *Bose-Einstein Condensation with High Atom number in a Deep Magnetic Trap*, PhD thesis, University of Amsterdam 2001

[19] H. Ludvigsen, M. Tossavinen ans M. Kaivola *Laser linewidth measurements using self-homodyne detection with short delay*, Optics Communications **155** (180) 1998

[20] D. J. Griffiths *Introduction to Electrodynamics*, Prentice Hall 1999

[21] W. Petrich, et. al, *Stable, Tightly Confining Magnetic Trap for Evaporative Cooling of Neutral Atoms*, **74** (3352) 1995

[22] D. E. Pritchard, *Cooling atoms in a magnetic trap for precision spectroscopy*, Physical Review Letters, **51** (1336) 1983

[23] O. J. Luiten *Lyman-α Spectroscopy of Magnetically Trapped Atomic Hydrogen*, PhD thesis, University of Amsterdam, 1993

[24] S. M. Barnett, E. Riis and M. Wilkinson *Quantum dynamics of simple systems*, IOP: Bristol, 1996

[25] O. J. Luiten et. al, *Kinetic theory of the evaporative cooling of a trapped gas*, Phys. Rev. A **53** (381) 1996

[26] E. Hodby, et. al, *Bose-Einstein condensation in a stiff TOP trap with adjustable geometry*, J. Phys. B. **33** (4087) 2000

[27] K. W. Madison, et. al, *Vortex Formation in a Stirred BEC*, Phys. Rev. Lett. **84** (806) 2000

[28] E. Hodby, et. al, *Vortex Nucleation in Bose Einstein Condensates in an Oblate, Purely Magnetic Potential*, Phys. Rev. Lett. **88** (010405) 2002

[29] C. J. Pethick and H. Smith, *Bose-Einstein condensation in dilute gases*,CUP, Cambridge (2002)

[30] E. P. Gross, Nuovo Cimento , **20** (454) 1961

[31] E. P. Gross, J. Math. Phys. , **4** (195) 1963

[32] L. P. Pitaevskii , Zh. Eksp. Theor. Fiz. **40** (646) 1961

[33] F. Dalvolvo, S. Giorgini, L. P. Pitaevskii and S. Stringari *Theory of Bose Einstein condensation in trapped gases*, Rev. Mod. Phys. **71** (463) 1999

[34] Y. Kagan, et. al, *Evolution of a Bose condensed gas under variations of the confining potential*, Phys. Rev. A. **54** (1753) 1996

[35] Y. Castin, et. al, *Bose Einstein condensation in time dependent traps*, Phys. Rev. Lett. **77** (5315) 1996

[36] M. R. Andrews, et. al, *Observation of Interference Between Two Bose Einstein Condensates*, Science **275** (637) 1997

[37] C. Raman, et. al, *Evidence for a Critical Velocity in a Bose Einstein Condensed gas*, Phys. Rev. Lett. **83** (2502) 1999

[38] J. Stenger, et. al, *Bragg Spectroscopy of a Bose Einstein Condensate*, Phys. Rev. Lett. **82** (4569) 1999